

Finsler geometry modeling and Monte Carlo study of skyrmion shape deformation by uniaxial stressSahbi El Hog,¹ Fumitake Kato,² Hiroshi Koibuchi^{3,*} and Hung T. Diep^{4,†}¹*Laboratoire de la Matière Condensée et des Nanosciences (LMCN), Université de Monastir, Département de Physique, Faculté des Sciences de Monastir, Avenue de l'Environnement, 5019 Monastir, Tunisia*²*Department of Industrial Engineering, National Institute of Technology (KOSEN), Ibaraki College, Nakane 866, Hitachinaka, Ibaraki 312-8508, Japan*³*National Institute of Technology (KOSEN), Sendai College, 8 Nodayama, Medeshima-Shiote, Natori-shi, Miyagi 981-1239, Japan*⁴*Laboratoire de Physique Théorique et Modélisation, CY Cergy Paris University, CNRS, UMR 8089 2, Avenue Adolphe Chauvin, 95302 Cergy-Pontoise Cedex, France*

(Received 7 March 2021; revised 14 May 2021; accepted 22 June 2021; published 1 July 2021)

Skyrmions in chiral magnetic materials are topologically stable and energetically balanced spin configurations appearing under the presence of ferromagnetic interaction (FMI) and Dzyaloshinskii-Moriya interaction (DMI). Much of the current interest has focused on the effects of magnetoelastic coupling on these interactions under mechanical stimuli, such as uniaxial stresses for future applications in spintronics devices. Recent studies suggest that skyrmion shape deformations in thin films are attributed to an anisotropy in the coefficient of DMI, such that $D_x \neq D_y$, which makes the ratio λ/D anisotropic, where the coefficient of FMI λ is isotropic. It is also possible that $\lambda_x \neq \lambda_y$ while D is isotropic for λ/D to be anisotropic. In this paper, we study this problem using a modeling technique constructed based on Finsler geometry (FG). Two possible FG models are examined: In the first (second) model, the FG modeling prescription is applied to the FMI (DMI) Hamiltonian. We find that these two different FG models' results are consistent with the reported experimental data for skyrmion deformation. We also study responses of helical spin orders under lattice deformations corresponding to uniaxial extension/compression and find a clear difference between these two models in the stripe phase, elucidating which interaction of FMI and DMI is deformed to be anisotropic by uniaxial stresses.

DOI: [10.1103/PhysRevB.104.024402](https://doi.org/10.1103/PhysRevB.104.024402)**I. INTRODUCTION**

Skyrmions are topologically stable spin configurations [1–6] observed in chiral magnetic materials such as FeGe, MnSi, etc. [7–11], and are considered to be applicable for future spintronics devices [12]. For this purpose, many experimental and theoretical studies have been conducted [13–16], specifically on responses to external stimuli such as mechanical stresses [17–24]. It has been demonstrated that mechanical stresses stabilize/destabilize or deform the skyrmion configuration [25–29].

Effects of magnetostriction of chiral magnets are analytically studied using spin density waves by a Landau-type free-energy model, in which magnetoelastic coupling (MEC) is assumed [30–32]. In a micromagnetic theory based on chiral symmetry breaking, anisotropy in the exchange coupling is assumed in addition to a magnetostriction term to implement nontrivial effects on helical states and stabilize skyrmions [21,22]. Using such a model implementing MEC into Ginzburg-Landau free energy, Wang *et al.* reported simulation data for spins' responses under uniaxial stresses [33], and their results accurately explain

both the skyrmion deformation and alignment of helical stripes.

Among these studies, Shibata *et al.* reported an experimental result of large deformation of skyrmions by uniaxial mechanical stress, and they concluded that the origin of this shape deformation is an anisotropy in the coefficient D of Dzyaloshinskii-Moriya interaction (DMI), such that $D_x \neq D_y$ [34]. Such an anisotropic DMI can be caused by uniaxial mechanical stresses, because the origin of DMI anisotropy is a spin-orbit coupling [12]. It was reported in Ref. [35] that this anisotropy in D comes from a quantum mechanical effect of interactions between electrons and atoms resulting from small strains. Moreover, skyrmion deformation can also be explained by a DMI anisotropy in combination with antiferromagnetic exchange coupling [36,37].

However, we have another possible scenario for skyrmion deformation; it is an anisotropy in the FMI coefficient λ such that $\lambda_x \neq \lambda_y$. This direction-dependent λ causes an anisotropy λ/D even for isotropic D as discussed in Ref. [34], although the authors concluded that anisotropy λ/D comes from anisotropy in D . Such an anisotropy in λ , the direction-dependent coupling of FMI, also plays an important role in the domain wall orientation [38].

Therefore, it is interesting to study which coefficient of FMI and DMI should be anisotropic for the skyrmion deformation and stripe alignment by a geometric modeling technique. On the stripe alignment, Dho *et al.* experimentally

*koi-hiro@sendai-nct.ac.jp; koibuchih@gmail.com

†diep@cyu.fr

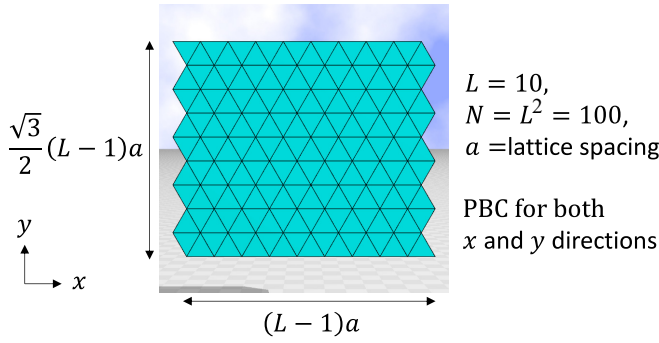


FIG. 1. A regular triangular lattice of size $N=L^2=100$, where the total number of vertices is $L=10$ along each of the edges. This number, $L=10$, is fixed to be very small to visualize the lattice structure. Simulations are performed on a lattice of size $N=10^4$. Periodic boundary condition (PBC) is assumed in both directions. The lattice spacing a is fixed to $a=1$ in the simulations.

studied the magnetic microstructure of an $\text{La}_{0.7}\text{Sr}_{0.3}\text{MnO}_3$ (LSMO) thin film and reported magnetic-force microscope images under tensile/compressive external forces [39].

In this paper, using Finsler geometry (FG) modeling, which is a mathematical framework for describing anisotropic phenomena [40–42], we study two possible models for the deformation of skyrmions and the alignment of magnetic stripes [43]. In one of the models, the FMI coefficient is deformed to be $\lambda_x \neq \lambda_y$, while DMI is isotropic, and in the other model, the DMI coefficient is deformed to be $D_x \neq D_y$, while FMI is isotropic. Both model 1 and model 2 effectively render the ratio λ/D anisotropic for modulated states, implying that a characteristic length scale is also rendered to be anisotropic [22]. Note also that the present FG prescription cannot directly describe an anisotropic magnetization expected from MEC. In this sense, FG models in this paper are different from both the standard Landau-type model of MEC and micromagnetic theory for thin films studied in Ref. [22,30–32], although these standard models implement MEC by an extended anisotropy of FMI in the sense that a magnetization anisotropy or higher order term of magnetization is included in addition to the exchange anisotropy.

II. MODELS

A. Triangular lattices

We use a triangular lattice composed of regular triangles of side length a , called lattice spacing [44] (Fig. 1). Triangular lattices are used for simulating skyrmions on thin films [45,46], where a frustrated system or antiferromagnetic interaction is assumed for studying possible mechanisms of skyrmion formation on chiral magnetic materials. However, the purpose in this paper is not the same as in Refs. [45,46]. On the other hand, skyrmions are known to be stabilized on thin films [24]. On the thin film of MnSi, hexagonal skyrmion crystal is observed, which can be realized on the triangular lattice. This is one of the reasons why we use triangular lattice, though the results in this paper are expected to remain unchanged on the regular square lattice because ferromagnetic

interaction is assumed, or in other words, the system is not frustrated.

The lattice size N , which is the total number of vertices, is given by $N=L^2$, where $L-1$ is the total number of triangles in both horizontal and vertical directions. The side length of the lattice is $(L-1)a$ along the vertical direction and $(\sqrt{3}/2)(L-1)a$ along the horizontal direction. Boundary conditions for dynamical variables are assumed to be periodic in both directions, as assumed in 3D simulations in Ref. [14]. Skyrmions are topological solitons which depend on the boundary condition. The boundary condition also strongly influences skyrmions in motion such as those in transportation. However, in our simulations, every skyrmion is only allowed to thermally fluctuate around a fixed position. For this reason, to avoid unexpected boundary effects, we assume the periodic boundary condition.

The lattice spacing is fixed to $a=1$ for simplicity, and the lattice size is fixed to $N=10^4$ for all simulations. As we describe in Sec. III, the numerical results are completely independent of the lattice size up to 400×400 at the boundary region between skyrmion and ferromagnetic phases and, therefore, all simulations are performed on the lattice of size 100×100 .

B. The Hamiltonian and a new variable for mechanical strains

The discrete Hamiltonian is given by the linear combination of five terms such that

$$S = \lambda S_{\text{FM}} - S_B + D S_{\text{DM}} + \gamma S_\tau - \alpha S_f, \quad (\alpha = 1), \quad (1)$$

where FMI and DMI energies S_{FM} and S_{DM} are given in two different combinations denoted by model 1 and model 2 [43] (see Appendix A),

$$\begin{aligned} S_{\text{FM}} &= \sum_{\Delta} [\lambda_{ij}(1 - \sigma_i \cdot \sigma_j) + \lambda_{jk}(1 - \sigma_j \cdot \sigma_k) \\ &\quad + \lambda_{ki}(1 - \sigma_k \cdot \sigma_i)], \\ \lambda_{ij} &= \frac{1}{3} \left(\frac{v_{ij}}{v_{ik}} + \frac{v_{ji}}{v_{jk}} \right), \quad v_{ij} = |\tau_i \cdot \vec{e}_{ij}| + v_0, \quad (\text{model 1}), \\ S_{\text{DM}} &= \sum_{ij} \vec{e}_{ij} \cdot \sigma_i \times \sigma_j, \end{aligned} \quad (2)$$

and

$$\begin{aligned} S_{\text{FM}} &= \sum_{ij} (1 - \sigma_i \cdot \sigma_j), \\ S_{\text{DM}} &= \sum_{\Delta} [\lambda_{ij}(\vec{e}_{ij} \cdot \sigma_i \times \sigma_j) + \lambda_{jk}(\vec{e}_{jk} \cdot \sigma_j \times \sigma_k) \\ &\quad + \lambda_{ki}(\vec{e}_{ki} \cdot \sigma_k \times \sigma_i)], \\ \lambda_{ij} &= \frac{1}{3} \left(\frac{v_{ij}}{v_{ik}} + \frac{v_{ji}}{v_{jk}} \right), \quad v_{ij} = \sqrt{1 - (\tau_i \cdot \vec{e}_{ij})^2} + v_0, \end{aligned} \quad (\text{model 2}), \quad (3)$$

where FG modeling prescription is only applied to S_{FM} (S_{DM}) in model 1 (model 2). Note that S_{FM} in model 1 and S_{DM} in model 2 are defined by the sum over triangles \sum_{Δ} . The coefficients λ and D of S_{FM} and S_{DM} represent the strength of FMI and DMI. The coefficients λ_{ij} inside the sum \sum_{Δ} of S_{FM} and S_{DM} are obtained by discretization of the corresponding

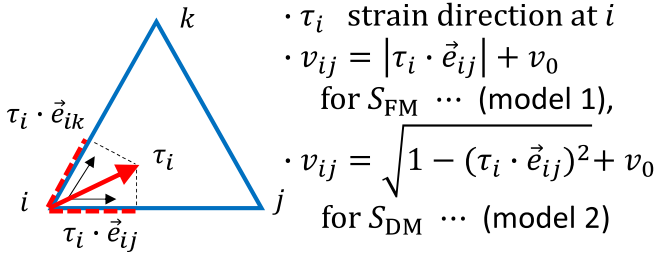


FIG. 2. A regular triangle of vertices i, j, k , and a strain direction τ_i at vertex i . The unit Finsler length v_{ij} from vertices i to j is defined by using the tangential component $\tau_i \cdot \bar{e}_{ij}$ of τ_i along the direction \bar{e}_{ij} , which is the unit tangential vector from i to j .

continuous Hamiltonians with Finsler metric (see Appendix A). i, j, k of v_{ij} in λ_{ij} denote the three vertices of the triangle (Fig. 2).

The symbol $\sigma_i (\in S^2$: unit sphere) denotes the spin variable at lattice site i , which is a vertex of the triangle. The symbol $\tau_i (\in S^1$: unit circle) in v_{ij} denotes a direction of strain. Microscopically, strains are understood to be connected to a displacement of atoms, which also thermally fluctuate or vibrate without external forces. Thus, an internal variable can be introduced to represent the direction of movement or position deformation of atom i . For this reason, τ_i is introduced in models 1 and 2. A random or isotropic state of τ_i effectively corresponds to a zero-stress or zero-strain configuration, while an aligned state corresponds to a uniaxially stressed or strained configuration. The zero-strain configuration includes a random and inhomogeneous strain configuration caused by a random stress, because the mean value of random stress is effectively identical with zero stress from the microscopic perspective. We should note that the variable τ_i is expected to be effective only in a small stress region to represent strain configurations ranging from random state to aligned state. In fact, if the variables once align along an external force direction, which is sufficiently large, no further change is expected in the configuration. Therefore, the strain representation by τ_i is effective only in a small stress or strain region.

One more point to note is that the variable τ is assumed to be nonpolar in the sense that it is only direction dependent and independent of the positive/negative direction. Indeed, the direction of τ is intuitively considered to be related to whether the external mechanical force is tension or compression. However, to express an external tensile force, we need two opposite directions in general. This assumption ($\Leftrightarrow \tau$ is nonpolar) is considered sufficient because the interaction, implemented via v_{ij} in Eqs. (2) and (3) for λ_{ij} , is simply dependent on $|\tau_i \cdot \bar{e}_{ij}|$ and $(\tau_i \cdot \bar{e}_{ij})^2$, respectively, where \bar{e}_{ij} is the unit tangential vector from vertex i to vertex j and, hence, the interaction is dependent only on strain directions and independent of whether τ is polar or nonpolar.

We should note that λ_{ij} and $D\lambda_{ij}$ in the FMI and DMI are considered to be microscopic interaction coefficients, which are both position ($\Leftrightarrow i$) and direction ($\Leftrightarrow ij$) dependent. The expression of λ_{ij} of model 1 is the same as that of model 2, and the relation $\lambda_{ij} = \lambda_{ji}$ is automatically satisfied. However, the definitions of v_{ij} are different from each other. Hence, the value of λ_{ij} of model 1 is not always identical to that of model

2. Indeed, if τ_i is almost parallel to the x axis (see Fig. 2), v_{ij} is relatively larger (smaller) than v_{ik} and v_{jk} in model 1 (model 2) and, as a consequence, λ_{ij} also becomes relatively large (small) compared with the case where τ_i is perpendicular to the x axis.

To discuss this point further, we introduce effective coupling constants of DMI such that

$$\langle D_x \rangle = (1/N_B) \sum_{ij} \lambda_{ij} |\bar{e}_{ij}^x|, \quad (4)$$

$$\langle D_y \rangle = (1/N_B) \sum_{ij} \lambda_{ij} |\bar{e}_{ij}^y|,$$

where \bar{e}_{ij}^x and \bar{e}_{ij}^y are components of $\bar{e}_{ij} = (\bar{e}_{ij}^x, \bar{e}_{ij}^y) \in \mathbf{R}^2$, which is the unit tangential vector from vertex i to vertex j as mentioned above, and $N_B = \sum_{ij} 1 (= 3N)$ is the total number of links or bonds. Expressions of $\langle \lambda_x \rangle$ and $\langle \lambda_y \rangle$ for FMI are exactly the same as those of $\langle D_x \rangle$ and $\langle D_y \rangle$ in Eqs. (4). The symbol $\langle \cdot \rangle$ for the mean value is henceforth removed for simplicity. Suppose the effective coupling constants λ_x and λ_y , for S_{FM} in model 1 satisfy $\lambda_x > \lambda_y$. In this case, the resulting spin configurations are expected to be the same as those in model 2 under $D_x < D_y$ for S_{DM} because an skx configuration emerges as a result of competition between S_{FM} and S_{DM} . This is an intuitive understanding that both models are expected to have the same configuration in the skx phase. If λ_{ij} is isotropic or locally distributed at random, almost independent of the direction ij , then the corresponding microscopic coupling constants $\lambda_{ij} |\bar{e}_{ij}^x|$ and $\lambda_{ij} |\bar{e}_{ij}^y|$ in D_x and D_y of Eqs. (4) also become isotropic and, consequently, $D_x = D_y$ is expected. In contrast, if the variable τ is aligned by the external force \vec{f} , then λ_{ij} becomes anisotropic or globally direction dependent and, as a consequence, D_x and D_y become anisotropic such that $D_x \neq D_y$.

We should comment that our models include a shear component of stress effect on the coefficient λ_{ij} in Eqs. (2) and (3). To simplify arguments, we tentatively assume $v_0 = 0$ in model 1. Let \vec{f} be $\vec{f} = (f, 0)$ or parallel to \bar{e}_{ij} , which represents the first local coordinates axis (Fig. 2), implying that τ_i is almost parallel to \bar{e}_{ij} for sufficiently large f . Then, we have $v_{ij} \simeq |\tau_i| = 1$, which represents an effect of the tensile stress \vec{f} along \bar{e}_{ij} . For the same τ_i , we have $v_{ik} \simeq 0.5 |\tau_i| = 0.5$ along \bar{e}_{ik} , which represents the second local coordinate axis. Thus, we obtain the ratio $v_{ij}/v_{ik} \simeq 2$, and by moving the local coordinate origin to vertex j and from the same calculation, we obtain $v_{jk}/v_{ji} \simeq 2$ and, therefore, $\lambda_{ij} = 4/3$. Since the variables τ at all other vertices are naturally considered to be parallel to \bar{e}_{ij} , we have $\lambda_{ik} = 1/3$ from the same argument. The fact that λ_{ik} is nonzero under $\vec{f} = (f, 0)$ is considered to be an effect of shear stress.

The other terms S_B , S_τ , and S_f in S of Eq. (1) are common to both models and are given by

$$S_B = \sum_i \sigma_i \cdot \vec{B}, \quad \vec{B} = (0, 0, B),$$

$$S_\tau = \frac{1}{2} \sum_{ij} (1 - 3(\tau_i \cdot \tau_j)^2), \quad S_f = \sum_i (\tau_i \cdot \vec{f})^2,$$

$$\vec{f} = (f_x, f_y), \quad (5)$$

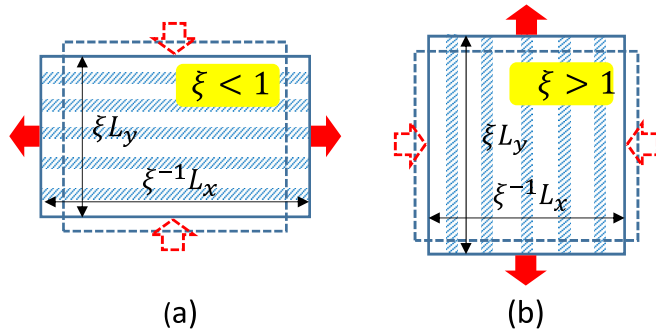


FIG. 3. Lattice deformations represented by (a) $\xi < 1$ and (b) $\xi > 1$ in Eqs. (6). In (a) for $\xi < 1$ and (b) for $\xi > 1$, the corresponding external tensile forces' direction is horizontal and vertical, respectively. The dashed arrows represent the direction of forces, implying that the force is assumed compressive, and the shaded thick lines denote the stripe directions experimentally observed and reported in Ref. [39].

where S_B is the Zeeman energy with magnetic field \vec{B} , and S_τ is a Lebwohl-Lasher type potential [47], which is always assumed for models of liquid crystals [41].

In S_f , $\vec{f} = (f_x, f_y)$ represents an external mechanical force, which aligns the strain direction τ along the direction of \vec{f} . The reason why S_f is not linear concerning \vec{f} (or τ) is that the force \vec{f} has a non-polar interaction given by S_τ . Therefore, it is natural to assume the square type potential. In liquid crystals, such a square type potential is also assumed for external electric fields [41]. The coefficient α of S_f in Eq. (1) is fixed to $\alpha = 1$ for simplicity. This is always possible by re-scaling f to $\sqrt{\alpha}f$.

Alignment of the direction of τ is essential for modeling the stress effect in models 1 and 2. In this paper, we assume the following two different sources for this alignment:

- (i) Uniaxial stresses by $\vec{f} = (f, 0)$ and $\vec{f} = (0, f)$ with $\gamma = 0$ (for skyrmion deformation),
- (ii) Uniaxial strains by lattice deformation by ξ with $\gamma > 0$ (for stripe deformation),

where ξ in (ii) is defined by the deformations of side lengths such that (Fig. 3)

$$L_x \rightarrow \xi^{-1}L_x, \quad L_y \rightarrow \xi L_y, \quad (6)$$

where $f > 0$ is assumed, implying that \vec{f} is tensile, and L_x and L_y are actually given by $L_x = (L-1)a$ and $L_y = (\sqrt{3}/2)(L-1)a$ as shown in Fig. 1. In both cases (i) and (ii), the variable τ is expected to be aligned, and this alignment causes deformations in the interactions of S_{FM} and S_{DM} to be direction dependent like in the forms $\lambda\lambda_{ij}$ and $D\lambda_{ij}$ as mentioned above. In case (i), the lattice is undeformed, implying that ξ is fixed to $\xi = 1$. In case (i), uniaxial stresses by the external force are only applied to check the skyrmion shape deformation, and the coupling constant γ of S_τ is assumed to be $\gamma = 0$. On the contrary, in case (ii), the external force \vec{f} is assumed to be ineffective and fixed to $\vec{f} = (0, 0)$, while the parameter γ for S_τ is fixed to a non-negative constant $\gamma > 0$ so τ can spontaneously align to a certain direction associated with the lattice deformation by ξ . In case (ii), S_{DM} is expected to play a nontrivial role in both models 1 and 2 because lattice

TABLE I. List of symbols and descriptions of the input parameters.

Symbol	Description
T	Temperature
λ	Ferromagnetic interaction coefficient
D	Dzhaloshinskii-Moriya interaction coefficient
B	Magnetic field
γ	Interaction coefficient of S_τ
f	Strength of mechanical force $\vec{f} = (f, 0)$ or $\vec{f} = (0, f)$ with $f > 0$
v_0	Strength of anisotropy
Symbol	Description (assumed typical value)
ξ	Deformation parameter for the side lengths of lattice: $\xi = 1 \Leftrightarrow$ nondeformed

deformations originally influence DMI. This will be a check on whether or not a coupling of strain and spins (or magnetization) is effectively implemented in DMI. It is clear that S_{FM} of model 2 in Eqs. (3) is completely independent of the lattice deformation by ξ .

The partition function is defined by

$$Z = \sum_{\sigma} \sum_{\tau} \exp[-S(\sigma, \tau)/T], \quad (7)$$

where \sum_{σ} and \sum_{τ} denote the sum over all possible configurations of σ and τ , and T is the temperature. Note that the Boltzmann constant k_B is assumed to be $k_B = 1$.

Here, we show the input parameters for simulations in Table I.

C. Monte Carlo technique and snapshots

The standard Metropolis Monte Carlo (MC) technique is used to update the variables σ and τ [48,49]. For the update of σ , a new variable σ'_i at vertex i is randomly generated on the unit sphere S^2 independent of the old σ_i and, therefore, the rate of acceptance is not controllable. The variable τ is updated on the unit circle S^1 by almost the same procedure as that of σ .

The initial configuration of spins is generated by searching the ground state (see Ref. [50]). One MC sweep (MCS) consists of N consecutive updates of σ and that of τ . In almost all simulations, 2×10^8 MCSs are performed. At the phase boundary between the skyrmion and ferromagnetic phases, the convergence is relatively slow, and therefore 5×10^8 MCSs or more, up to 1.6×10^9 MCSs, are performed. In contrast, a relatively small number of MCSs are performed in the ferromagnetic phase at large $|B|$ or high T region. Here, we show snapshots of skyrmion configuration obtained by model 2 for $f = 0$ and $f \neq 0 (= 1.7)$ in Figs. 4(a) and 4(b). The assumed parameters other than f are $T = 0.2$, $D = 0.45$, $\gamma = 0$, $v_0 = 0.7$, and $\xi = 1$ for both (a) and (b). The cones represent spins σ_i , and the colors of cones correspond to z -component σ_i^z . We find from both snapshots that the direction of cones in the central region of skyrmions is $-z$ while it is $+z$ outside. Skyrmion configurations of model 1 are the same as these snapshots. This vortexlike configuration [Fig. 4(a)] is called Bloch type and symmetric under rotation along the z axis [51]. In this paper, we study skyrmions of Bloch type.

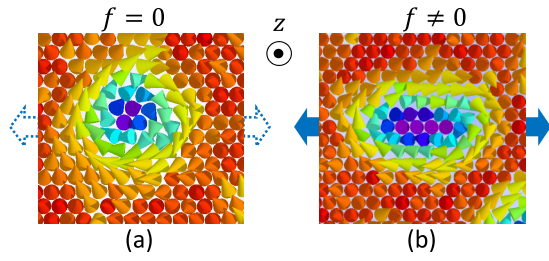


FIG. 4. Snapshot of skyrmions for (a) $f=0$ and (b) $f\neq 0(=1.7)$ with $T=0.2$, $D=0.45$, $\gamma=0$, $v_0=0.7$, and $\xi=1$. These snapshots are obtained by model 2 and the same as those obtained by model 1. This vortexlike skyrmion is called Bloch type, which is studied in this paper.

III. SIMULATION RESULTS

A. Responses to uniaxial stress

1. Magnetic field versus temperature diagram

A phase diagram of model 1 is shown in Fig. 5(a), where the temperature T and magnetic field B are varied. The symbols skx, str, and ferro denote the skyrmion, stripe, and ferromagnetic phases, respectively. The stripe phase is the same as the so-called helical phase, where the spins are rotating along the axis perpendicular to the stripe direction. Be-

tween these two different phases, intermediate phases appear, denoted by the skyrmion ferromagnetic (sk-fe) and skyrmion stripe (sk-st) phases. The parameters λ , D , γ , f , v_0 are fixed to $(\lambda, D, \gamma, f, v_0) = (0.8, 0.9, 0, 0.5, 0.15)$ in Fig. 5(a). The applied mechanical stress is given by $\vec{f} = (0.5, 0)$, which implies that a thin film is expanded in the x direction by a tensile force $f=0.5$.

The phase diagram in Fig. 5(a) is only a rough estimate for identifying the regions of different states. These boundaries are determined by viewing their snapshots. For example, if a skyrmion is observed in the final ferromagnetic configuration of simulation at the boundary region between the skx and ferro phases, this state is written as sk-fe. If two skyrmion states are connected to be an oblong shape and all others are isolated in a snapshot, then this state is written as sk-st. Thus, the phase boundaries in these digital phase diagrams are not determined by the standard technique such as the finite scaling analyses [50,52] and, therefore, the order of transition between two different states is not specified.

Figure 5(b) shows a snapshot of deformed skyrmions of model 1 at a relatively low temperature $T=0.1$. To measure the shape anisotropy, we draw rectangles enclosing skyrmions, as shown in Fig. 5(c), where the edge lines are drawn parallel to the x and y directions. The details of how the edge lines are drawn can be found in Appendix B. This

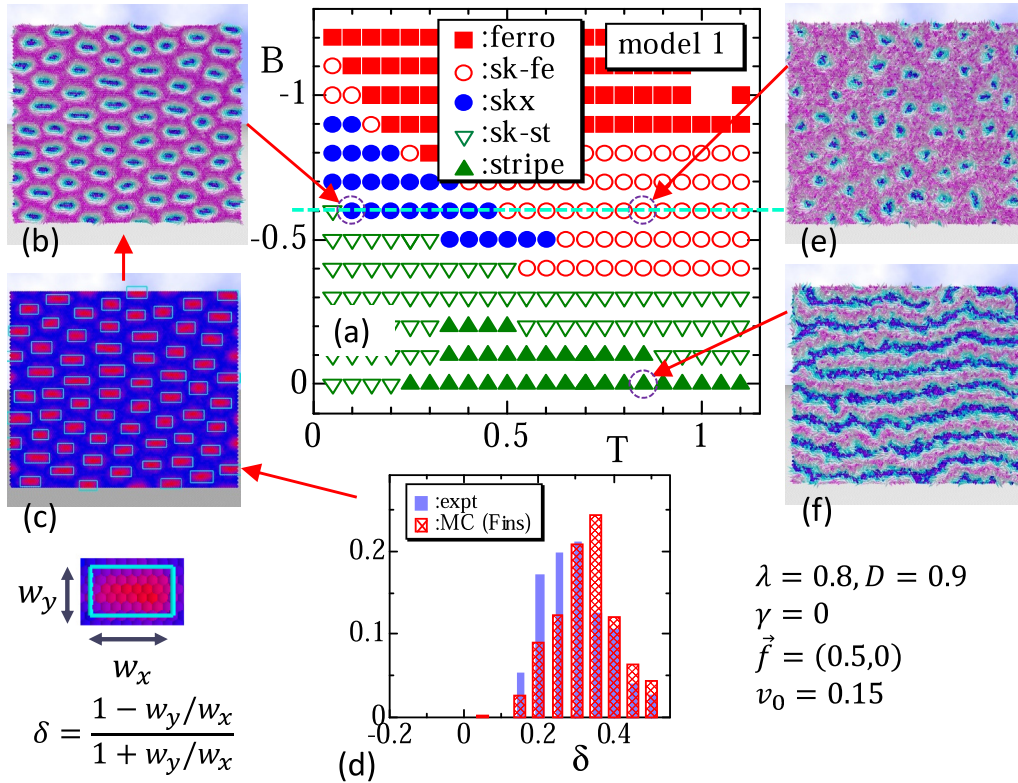


FIG. 5. (a) Phase diagram of magnetic field B and temperature T of model 1, (b) snapshot obtained at $(B, T) = (-0.6, 0.1)$, (c) corresponding snapshot to measure the shape anisotropy δ of skyrmion, (d) histograms of δ , where a reported histogram (expt) for the experimental result in Ref. [34] is also plotted, (e) snapshot at $(B, T) = (-0.6, 0.85)$, and (f) snapshot in the stripe phase at $(B, T) = (0, 0.85)$. The symbols skx, str, and ferro denote skyrmion, stripe, and ferromagnetic phases, respectively. The symbols sk-fe and sk-st denote intermediate phases of skyrmion ferromagnetic and skyrmion stripe, respectively. On the dashed horizontal line, physical quantities are calculated in the following subsection.

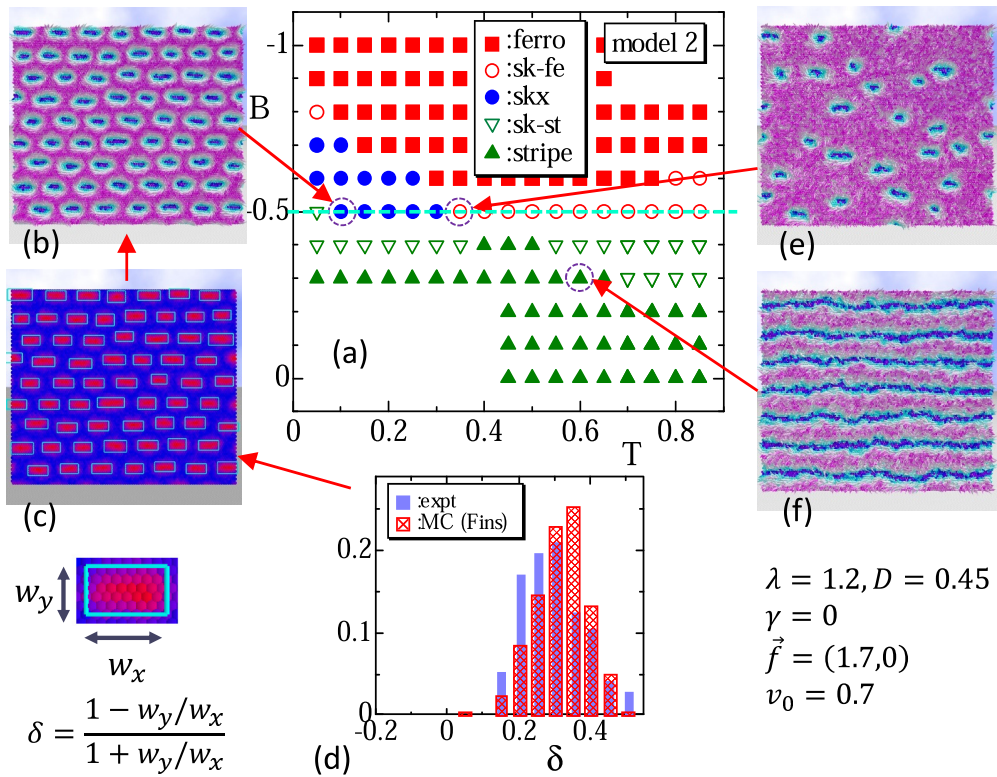


FIG. 6. (a) Phase diagram of magnetic field B and temperature T of model 2, (b) snapshot obtained at $(B, T) = (-0.5, 0.1)$, (c) corresponding snapshot to measure the shape anisotropy of the skyrmion, (d) the corresponding histogram of δ , where a reported histogram (expt) for the experimental result in Ref. [34] is also plotted, (e) snapshot at $(B, T) = (-0.5, 0.35)$, and (f) snapshot in the stripe phase at $(B, T) = (-0.3, 0.6)$. On the dashed horizontal line, physical quantities are calculated in the following subsection.

technique can also be used to count the total number of skyrmions, at least in the skx phase, which will be presented below. Figure 5(d) shows the distribution of shape anisotropy δ defined by

$$\delta = (1 - w_y/w_x)/(1 + w_y/w_x), \quad (8)$$

where w_x and w_y are the edge lengths of the rectangle [34]. The solid histogram is the experimental data (expt) reported in Ref. [34]. In Ref. [34], simulations were also performed by assuming that the DMI coefficients D are direction dependent such that $D_x/D_y = 0.8$, and almost the same result with expt was obtained. The result of model 1 in this paper, shown in the shaded histogram, is almost identical to that of expt. In these histograms, the height is normalized such that the total height remains the same. Another snapshot obtained at higher temperature $T = 0.8$ is shown in Fig. 5(e), where the shape of the skyrmion is not smooth and almost randomly fluctuating around the circular shape. Therefore, this configuration is grouped into the sk-fe phase, even though such fluctuating skyrmions are numerically stable, implying that the total number of skyrmions remains constant for long-term simulations. Figure 5(f) shows a snapshot obtained in the stripe phase. The direction of the stripes is parallel to the direction of the tensile force $\vec{f} = (f, 0)$.

The results of model 2 in Figs. 6(a)–6(f) are almost identical to those in Fig. 5. The parameters $\lambda, D, \gamma, f, v_0$ are fixed to $(\lambda, D, \gamma, f, v_0) = (1.2, 0.9, 0, 1.7, 0.7)$ in Fig. 6(a) for model 2. The unit of T depends on the ratio of T and

the coefficients of Hamiltonians $S_{FM}, S_B, S_{DM}, S_\tau$, and S_f . However, the ratios themselves cannot be compared with each other because the first two parameters, (λ, D) at least for model 1, are not proportional to these parameters for model 2. In fact, D in model 2 is effectively deformed to be direction dependent such that DD_x and DD_y by D_x and D_y in Eqs. (4), while D in model 1 remains unchanged. Therefore, the unit of the horizontal T axis in Fig. 5(a) is not exactly identical but almost comparable to that of model 1 in Fig. 6(a).

The parameter $v_0 = 0.7$ assumed in v_{ij} of Eqs. (3) for model 2 is relatively larger than $v_0 = 0.15$ in v_{ij} of Eqs. (2) for model 1. If v_0 in model 2 is fixed to be much smaller, such as $v_0 = 0.15$ just like in model 1, then the shape of the skyrmions becomes unstable. This fact implies that the anisotropy of DMI caused by the FG model prescription is too strong for such a small v_0 in model 2. Conversely, if v_0 in model 1 is fixed to be much larger, such as $v_0 = 0.7$, then the skyrmion shape deformation is too small, implying that anisotropy of FMI caused by the FG model prescription is too weak for $v_0 = 0.7$.

Here, we should note that the skx region in the BT diagrams of Figs. 5 and 6 changes with varying B at the relatively low T region. Indeed, if $|B|$ is increased from $B = 0$ at $T = 0.1$ in Fig. 6 for example, the connected stripes like in Fig. 6(f) start to break, and the stripe phase changes to sk-st at $|B| = 0.4$, and skx emerges at $|B| = 0.5$ as shown in Fig. 6(b). The skyrmion shape in the skx phase is oblong in the $(1, 0)$ direction, which is the same as the stripe direction for smaller B region. This shape anisotropy of skyrmions as well as the size itself becomes smaller and smaller with increasing $|B|$, and

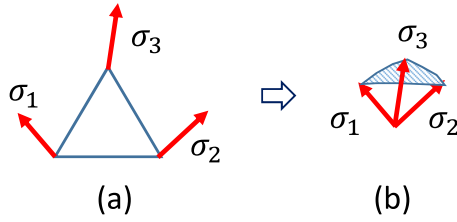


FIG. 7. (a) Spin variables $\sigma_i (i=1, 2, 3)$ at the three vertices of a triangle and (b) a small triangle area defined by $\sigma_i (i=1, 2, 3)$ on the unit sphere. This small area can be used to calculate the total number of skyrmions.

for sufficiently large $|B|$ such as $|B|=0.8$, the skx turns to be ferromagnetic.

2. Temperature dependence of physical quantities

The total number of skyrmions N_{sk} is defined by

$$N_{sk} = (1/4\pi) \int d^2x \sigma \cdot \frac{\partial \sigma}{\partial x_1} \times \frac{\partial \sigma}{\partial x_2}, \quad (\text{top}) \quad (9)$$

which can be calculated by replacing differentials with differences [53,54]. This N_{sk} is denoted by ‘‘top’’ and plotted in the figures below. Another numerical technique for calculating N_{sk} is to measure the solid angle of the triangle cone formed by σ_1, σ_2 , and σ_3 [Fig. 7(a)]. Let a_Δ be the area of the shaded region in Fig. 7(b) and N_{sk} can then be calculated by

$$N_{sk} = \frac{1}{4\pi} \sum_{\Delta} a_{\Delta}, \quad (\text{are}), \quad (10)$$

and this is denoted by ‘‘are.’’ One more technique to count N_{sk} is denoted by ‘‘gra,’’ which is a graphical measurement technique (see Appendix B).

Figure 8(a) shows the dependence of $|N_{sk}|$ of model 1 on the temperature variation at $B=-0.6$, where the absolute values of N_{sk} are plotted. These curves in Fig. 8(a) are obtained along the horizontal dashed line in Fig. 5(a). We find that $|N_{sk}|$ discontinuously reduces at $T \simeq 0.45$ and that the reduced $|N_{sk}|$ in the region $T > 0.45$ of top and are remain finite up to $T \simeq 1$. Because of this discontinuous change of $|N_{sk}|$, the skx phase of model 1 is divided into two regions at $T \simeq 0.45$. This skx phase at higher temperatures is numerically stable. However, N_{sk} evaluated graphically, denoted by gra, increases at $T \simeq 0.6$. This behavior of N_{sk} implies that the skx configuration is collapsed or multiply counted. Therefore, the skx configuration should be grouped into the sk-fe phase in this region, and we plot a dashed line as the phase boundary between the skx and sk-fe phases. The curves $|N_{sk}|$ of model 2 in Fig. 8(b) are obtained along the horizontal dashed line in Fig. 6(a) at $B=-0.5$ and we find that N_{sk} discontinuously reduces to $N_{sk} \simeq 0$. This reduction implies that the skx phase changes to the sk-fe or ferro phase at $T \simeq 0.3$ in model 2.

To see the internal configuration of the 2D nonpolar variable τ , we calculate the order parameter by

$$M_\tau = 2(\langle \sigma_x \rangle^2 - 1/2). \quad (11)$$

This M_τ continuously changes with respect to T [Fig. 8(c) for model 1], and no discontinuous change is observed. However, it is clear that τ is anisotropic (isotropic) in the temperature

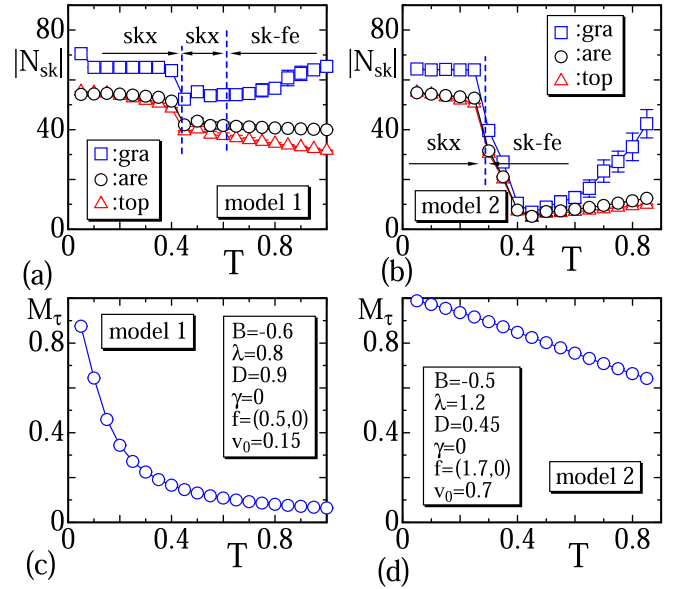


FIG. 8. Total number of skyrmions $|N_{sk}|$ of (a) model 1 and (b) model 2, where the gra, are, and top correspond to three different calculation techniques for $|N_{sk}|$; ‘gra’ denotes the graphical measurement technique presented in Appendix B, are and top denote the techniques of using the formulas in Eqs. (9) and (10). The corresponding order parameter M_τ of (c) model 1 and (d) model 2 is plotted.

region $T < 0.2$ ($0.5 < T$). The M_τ plotted in Fig. 8(d) for model 2 is very large compared with that in Fig. 8(c). This behavior of M_τ implies that τ is parallel to the direction of \vec{f} in the whole region of T plotted, resulting from the considerably large value of $f (= 1.7)$ assumed in model 2 for Fig. 6.

We should note that the variations of $|N_{sk}|$ with respect to T in Figs. 8(a) and 8(b) are identical to those (which are not plotted) obtained under $\vec{f} = (0, 0)$ and with the same other parameters. In this case, γ for S_τ is fixed to $\gamma = 0$ and, therefore, τ becomes isotropic. This result, obtained under $\vec{f} = (0, 0)$ and $\gamma = 0$, implies that the skyrmion deformation is caused by the alignment of τ , and the only effect of $\vec{f} \neq (0, 0)$ is to deform the skyrmion shape to anisotropic in the skx phase.

The DMI and FMI energies S_{DM}/N and S_{FM}/N are shown to have discontinuous changes at $T \simeq 0.4$ in both models [Figs. 9(a) and 9(b)], where N is the total number of vertices. The gaps of these discontinuities in S_{FM}/N are very small.

Anisotropy η_λ and η_D of effective FMI and DMI coefficients can be evaluated such that

$$\begin{aligned} \eta_\lambda &= 1 - \lambda_y/\lambda_x \quad (\text{model 1}), \\ \eta_D &= 1 - D_x/D_y \quad (\text{model 2}), \end{aligned} \quad (12)$$

where the expressions for D_x, D_y and λ_x, λ_y are given in Eqs. (4). The direction dependence of the definition η_λ of model 1 is different from η_D of model 2, and this difference comes from the fact that the definition of v_{ij} in Eqs. (2) for model 1 is different from that in Eqs. (3) of model 2. We find from the anisotropy η_λ of model 1 in Fig. 9(c) that η_λ is decreasing with increasing T , and this tendency is the same for η_D of model 2 in Fig. 9(d). It is interesting to note that η_D of model 2 is $\eta_D \simeq 0.2$ in the skx phase at $T < 0.4$.

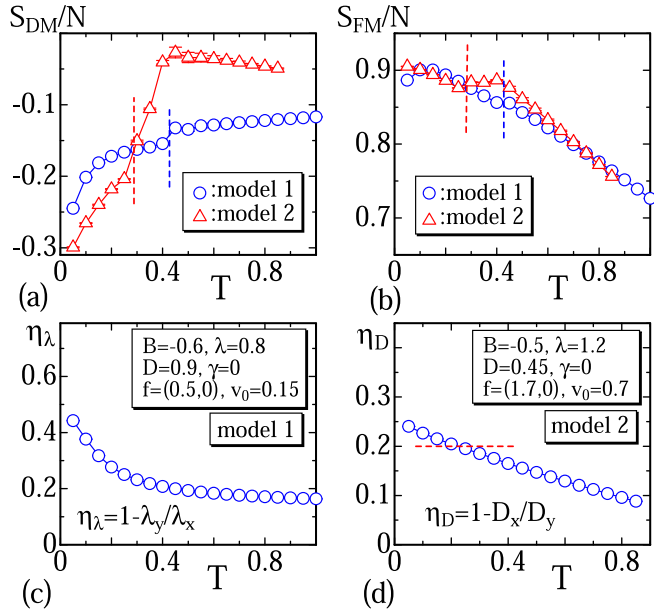


FIG. 9. (a) S_{DM}/N versus T of models 1 and 2, (b) S_{FM}/N versus T of models 1 and 2, the anisotropy of effective interaction coefficient η_λ and η_D versus T of (c) model 1 and (d) model 2. The vertical dashed lines in (a) and (b) roughly indicate the positions where S_{DM}/N and S_{FM}/N discontinuously change in models 1 and 2. The horizontal dashed line in (d) is drawn at $\eta_D = 0.2$, which is the value assumed in Ref. [34] to simulate the skyrmion deformation.

This value $\eta_D = 0.2$ corresponds to $D_x/D_y = 0.8$ explicitly assumed in Ref. [34] to simulate the skyrmion deformation. This η_D is slightly larger than 0.2 at $T \simeq 0.1$, where the shape anisotropy is comparable to the experimentally observed one, as demonstrated in Fig. 6(d). It must be emphasized that η_D or, equivalently, D_x and D_y of model 2, are not the input parameters for the simulations, where the input is \vec{f} , and the output is a skyrmion deformation like in the experiments.

Finally, in this subsection, we show how the simulations are convergent by plotting $|N_{sk}|$ (top) in Eq. (9) versus MCS and discuss how the stress influences the skx phase. The data $|N_{sk}|$ of model 1 plotted in Figs. 10(a)–10(c), which are obtained on the dashed line in Fig. 5 at the transition region $T \simeq 0.5$, indicate that the skyrmion number is independent of whether the stress is applied or not. This implies that the distortion of the FMI coefficient by uniaxial stress does not influence the skx and sk-fe phases. In contrast, we find in the remaining plots in Figs. 10(d)–10(f), which are obtained on the dashed line in Fig. 6, that $|N_{sk}|$ of model 2 depends on the stress. Indeed, $|N_{sk}|$ remains unchanged for the stressed condition in the skx phase [Fig. 10(d)], while $|N_{sk}|$ is considerably increased from $|N_{sk}| = \text{finite}$ in the sk-fe phase [Fig. 10(e)] and also from $|N_{sk}| = 0$ in the ferro phase [Fig. 10(f)]. It is interesting to note that such skyrmion proliferation is experimentally observed by uniaxial stress control not only in low-temperature region [19,27,28] but also in the high-temperature region close to the boundary with the ferro phase [20]. Thus, effects of uniaxial stress on skyrmion proliferation are considered to be implemented in model 2.

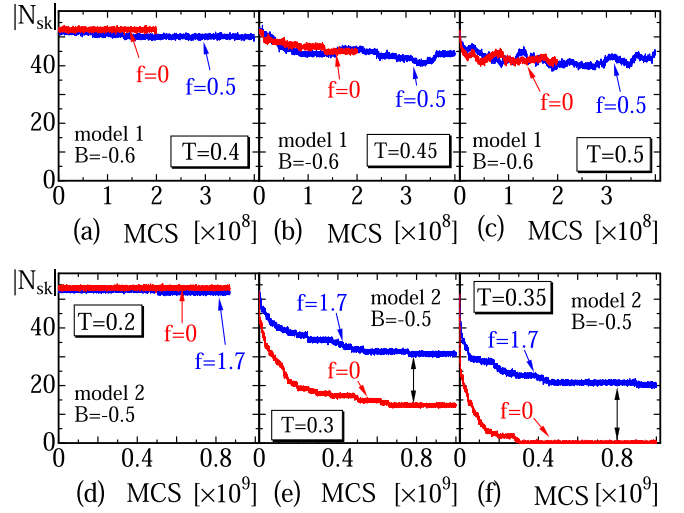


FIG. 10. $|N_{sk}|$ versus MCS obtained on the dashed lines in Figs. 5 and 6 at the boundary between skx and sk-fe phases in (a)–(c) model 1 and (d)–(f) model 2. $|N_{sk}|$ is independent of whether the stress is applied or not in model 1, while it clearly depends on the stress in model 2. The other parameters λ, D, γ, v_0 are the same as those shown in Figs. 5 and 6.

3. Stress versus magnetic field diagram

The external force f and magnetic field B are varied, and fB phase diagrams of models 1 and 2 are obtained (Figs. 11 and 12). The parameters are fixed to $(T, \lambda, D, \gamma, v_0) = (0.1, 0.8, 0.9, 0, 0.15)$ in Fig. 11 for model 1 and $(T, \lambda, D, \gamma, v_0) = (0.1, 1.2, 0.45, 0, 0.7)$ in Fig. 12 for model 2. The parameters $(\lambda, D, \gamma, v_0)$ for model 1 and model 2 are the same as those assumed for the BT phase diagrams in Figs. 5 and 6. The symbol (skx) for skyrmion and those for other phases are also exactly the same as those used in Figs. 5 and 6.

For the external force $\vec{f} = (f, 0)$ in the positive x direction, we assign positive f in the vertical axis of the diagrams. In the case of $\vec{f} = (f, 0)$ for positive f , the internal variable τ is expected to align along \vec{f} in the direction (1,0) or x direction. In contrast, the negative f in the diagrams means that $\vec{f} = (0, f)$. In this case, τ aligns along the direction (0,1) or y direction. Such an aligned configuration of τ along the y axis is also expected for $\alpha = -1$ with $\vec{f} = (f, 0)$ because the energy αS_f for $\alpha = 1$ with $\vec{f} = (0, f)$ is identical to αS_f for $\alpha = -1$ with $\vec{f} = (f, 0)$ up to a constant energy.

Figures 11(b) and 12(b) are snapshots of deformed skyrmions, where the shape anisotropy is slightly larger than the experimental one in Ref. [34]. In contrast, the snapshots in Figs. 11(c) and 12(c) are almost comparable in their anisotropy δ , as shown in Figs. 11(d) and 12(d) with the experimentally reported one denoted by expt. The word thinner, corresponding to the solid circle enclosed by a blue-colored square, indicates that the shape deformation is thinner than that of expt, and the word compa corresponding to that enclosed by a pink-colored diagonal indicates that the shape deformation is comparable to that of expt. For $f = 0$, the skyrmion shape is isotropic, as we see in Figs. 11(e) and 12(e), and the shape vertically deforms for the negative f region,

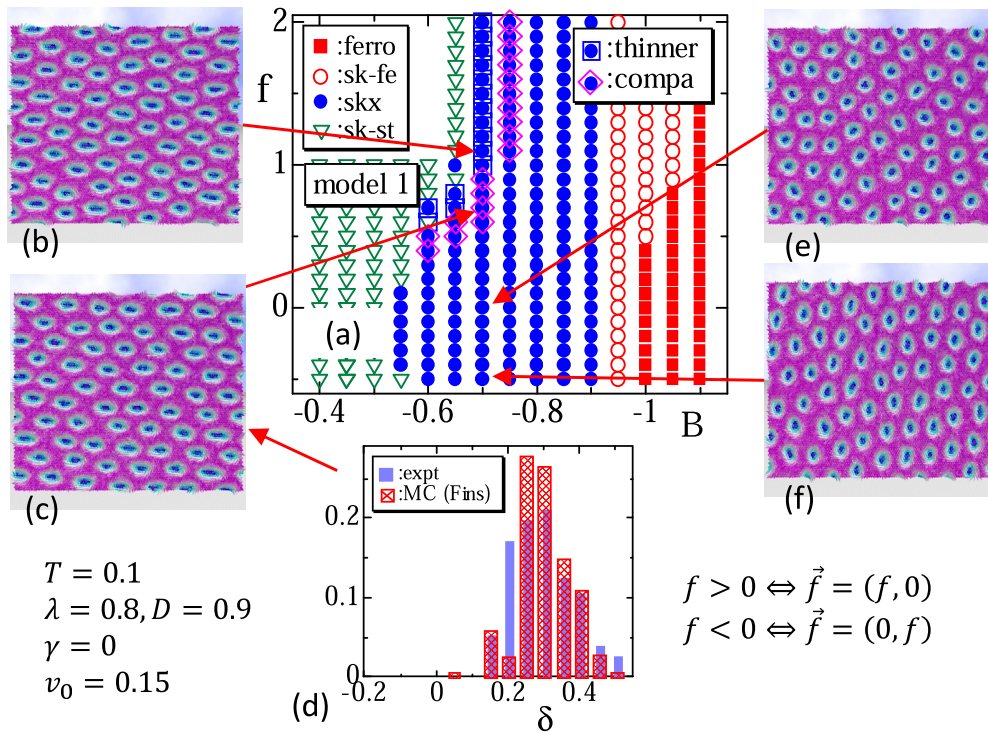


FIG. 11. (a) fB phase diagram of model 1, where f and B are the external force and magnetic field, (b) snapshot of skyrmions at $(f, B) = (1.1, -0.7)$, (c) snapshot obtained at $(f, B) = (0.7, -0.7)$, (d) histogram of δ corresponding to (c), which is close to expt data in Ref. [34], and (e), (f) snapshots obtained at $(f, B) = (0, -0.7)$ and $(f, B) = (-0.5, -0.7)$, where the negative f implies $\vec{f} = (0, f)$, and the skyrmion shape deforms vertically. The assumed parameter values are written in the figure.

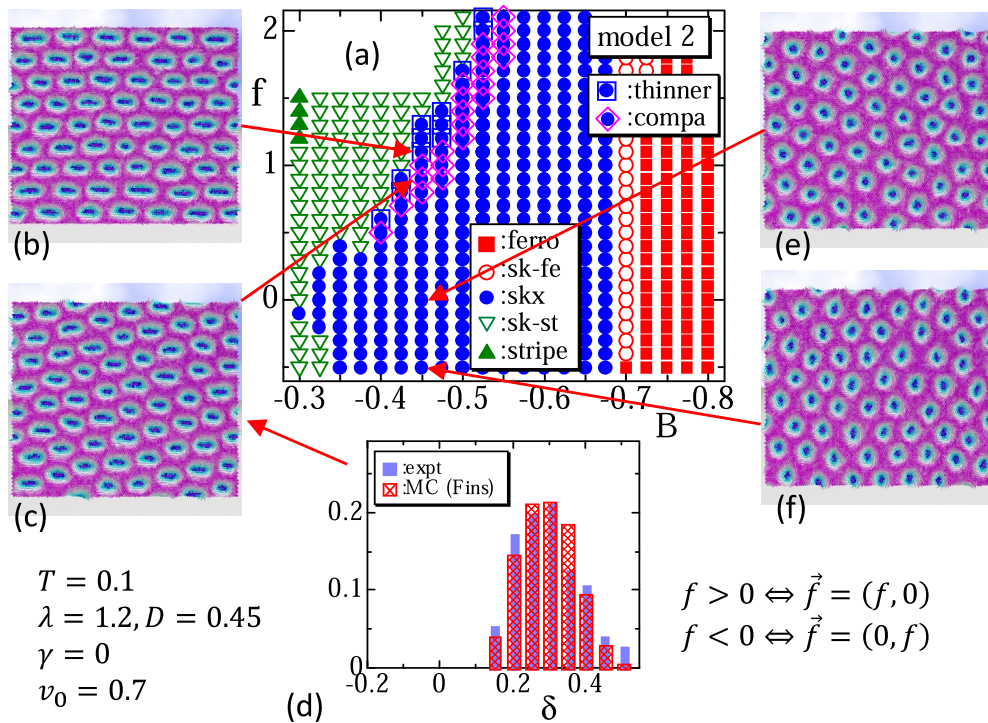


FIG. 12. (a) fB phase diagram of model 2, where f and B are the external force and magnetic field, (b) snapshot of skyrmions at $(f, B) = (1.1, -0.45)$, (c) snapshot obtained at $(f, B) = (0.9, -0.45)$, (d) histogram of δ corresponding to (c), which is close to expt data in Ref. [34], and (e), (f) snapshots obtained at $(f, B) = (0, -0.45)$ and $(f, B) = (-0.5, -0.45)$, where the negative f implies $\vec{f} = (0, f)$ and the skyrmion shape deforms vertically. The assumed parameter values are written on the figure.

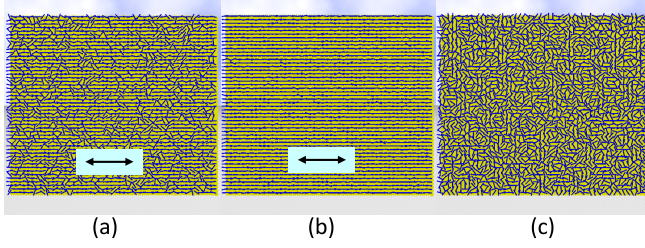


FIG. 13. Snapshots of τ corresponding to (a) Fig. 5(c) of model 1, (b) Fig. 6(c) of model 2, and (c) Fig. 12(e) of model 2. The small cylinders correspond to τ . The total number of cylinders is reduced to 2500, which is a quarter of $N(=10\,000)$, to clarify the directions. The arrows (\leftrightarrow) in (a) and (b) denote the direction of tensile force \vec{f} .

which implies positive f in $\vec{f}=(0, f)$, in Figs. 11(f) and 12(f). Thus, we can confirm from the snapshots that the shape deforms to oblong along the applied tensile force direction. Moreover, the deformation is almost the same as expt for a certain range of f in both models 1 and 2.

We should note that the skx phase changes to the sk-st phase with increasing f at a relatively small B region, however, it does not change to the ferro phase at an intermediate region of B even if f increases to sufficiently large, where τ saturates in the sense that no further change is expected. This saturation is because the role of \vec{f} is only to rotate the direction of τ . Hence, the modeling of stress by \vec{f} and τ is considered effective only in small stress regions, as mentioned in Sec. II. This point is different from the reported numerical results in Ref. [33], where the skx phase terminates, and the stripe or ferro phase appears for sufficiently large strain in the strain versus magnetic field diagram.

Finally, in this subsection, we show snapshots of the variable τ in Figs. 13(a)–13(c), which correspond to the configurations shown in Fig. 5(c) of model 1, Fig. 6(c) of model 2, and Fig. 12(e) of model 2, respectively. To clarify the directions of τ , we show a quarter of τ (\Leftrightarrow the total number of τ is 2500) in the snapshots. We find that τ is almost parallel to \vec{f} , denoted by the arrows in Fig. 13(a) and Fig. 13(b), and it is almost random in Fig. 13(c), where f is assumed to be $f=0$. The reason why τ in Fig. 13(b) is more uniform than in Fig. 13(a) is because $f(=1.7)$ in Fig. 13(b) is relatively larger than $f(=0.5)$ in Fig. 13(a).

B. Responses to uniaxial strains

To summarize the results in Sec. III A, both models 1 and 2 successfully describe the shape deformation of skyrmions under external mechanical forces \vec{f} . The skyrmion deformation comes from the fact that the skx phase is sensitive to the direction τ of the strain field influenced by f in $\vec{f}=(f, 0)$, which is assumed to be positive or equivalently tensile, as mentioned in Sec. II. This successful result implies that the interaction between spins and the mechanical force is adequately implemented in both models at least in the skx phase.

In addition, the response of spins in the stripe phase in both models or, more explicitly, the stripe direction as a response to \vec{f} , is also consistent with the reported experimental result in Ref. [39]. In Ref. [39], as mentioned in the introduction,

Dho *et al.* experimentally studied magnetic microstructures of LSMO thin film at room temperature and zero magnetic fields. The reported results indicate that the direction of the strain-induced magnetic stripe becomes dependent on whether the force is compression or tension.

On the other hand, the definition of S_{DM} in Eqs. (2) and (3) is explicitly dependent on the shape of the lattice and, therefore, we examine another check for the response of spins in the stripe phase by deforming the lattice itself, as described in Fig. 3. To remove the effect of \vec{f} , we fix \vec{f} to $f=0$ in S_f and, instead, γ in γS_τ is changed from $\gamma=0$ to $\gamma=0.5$ for model 1 and $\gamma=0.65$ for model 2. As a consequence of these nonzero γ , the variable τ is expected to align to some spontaneous directions. If the lattice deformation nontrivially influences τ , this spontaneously and locally oriented configuration of τ is expected to influence spin configurations strongly in the stripe phase. As a consequence, the stripe direction becomes anisotropic on deformed lattices ($\Leftrightarrow \xi \neq 1$), while the stripe is isotropic on the undeformed lattice ($\Leftrightarrow \xi = 1$).

To check these expectations by the lattice deformations shown in Fig. 3, we modify the unit tangential vector \vec{e}_{ij} , which originally comes from $\partial\vec{r}_i/\partial x_j$ (Appendix A). Indeed, $\partial\vec{r}_i/\partial x_j$ is understood to be the edge vector $\vec{\ell}_{ij}(=\vec{r}_j-\vec{r}_i)$ from vertex i to vertex j in the discrete model, and therefore, both the direction and the length of $\vec{\ell}_{ij}$ are changed by the lattice deformations in Fig. 3. Thus, the unit tangential vector $\vec{e}_{ij}=(e_{ij}^x, e_{ij}^y)$ in S_{DM} in Eqs. (2) and (3) is replaced by

$$\vec{e}'_{ij}=(e_{ij}^{\prime x}, e_{ij}^{\prime y})=(\xi^{-1}e_{ij}^x, \xi e_{ij}^y). \quad (13)$$

This generalized vector \vec{e}'_{ij} is identical to the original unit vector \vec{e}_{ij} for $\xi=1$. Note also that \vec{e}_{ij} in v_{ij} in Eqs. (2) and (3) is replaced by \vec{e}'_{ij} as follows:

$$\begin{aligned} S_{FM} &= \sum_{\Delta} [\lambda_{ij}(1 - \sigma_i \cdot \sigma_j) + \lambda_{jk}(1 - \sigma_j \cdot \sigma_k) \\ &\quad + \lambda_{ki}(1 - \sigma_k \cdot \sigma_i)], \\ S_{DM} &= \sum_{ij} \vec{e}'_{ij} \cdot \sigma_i \times \sigma_j, \\ \lambda_{ij} &= \frac{1}{3} \left(\frac{v_{ij}}{v_{ik}} + \frac{v_{ji}}{v_{jk}} \right), \\ v_{ij} &= \begin{cases} |\tau_i \cdot \vec{e}'_{ij}| + v_0 & (|\tau_i \cdot \vec{e}'_{ij}| < 1) \\ 1 + v_0 & (|\tau_i \cdot \vec{e}'_{ij}| \geq 1) \end{cases}, \quad (\text{model 1}), \end{aligned} \quad (14)$$

and

$$\begin{aligned} S_{FM} &= \sum_{ij} (1 - \sigma_i \cdot \sigma_j), \\ S_{DM} &= \sum_{\Delta} [\lambda_{ij}(\vec{e}'_{ij} \cdot \sigma_i \times \sigma_j) + \lambda_{jk}(\vec{e}'_{jk} \cdot \sigma_j \times \sigma_k) \\ &\quad + \lambda_{ki}(\vec{e}'_{ki} \cdot \sigma_k \times \sigma_i)], \\ \lambda_{ij} &= \frac{1}{3} \left(\frac{v_{ij}}{v_{ik}} + \frac{v_{ji}}{v_{jk}} \right), \\ v_{ij} &= \begin{cases} \sqrt{1 - (\tau_i \cdot \vec{e}'_{ij})^2} + v_0 & (|\tau_i \cdot \vec{e}'_{ij}| < 1) \\ v_0 & (|\tau_i \cdot \vec{e}'_{ij}| \geq 1) \end{cases}, \quad (\text{model 2}), \end{aligned} \quad (15)$$

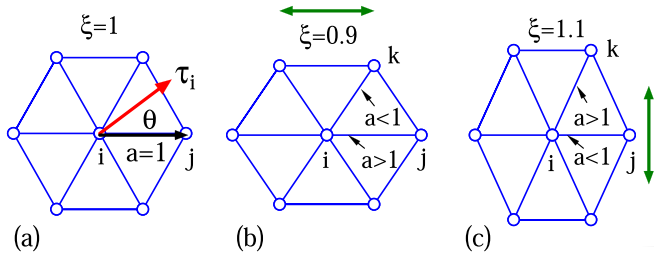


FIG. 14. (a) Regular triangular lattice corresponding to $\xi = 1$, and deformed lattices corresponding to (b) $\xi = 0.9$ and (c) $\xi = 1.1$. The bond length a in (a) is $a = 1$, while in (b) and (c), a changes to $a > 1$ or $a < 1$ depending on the direction of bonds. The symbol θ in (a) is the angle between τ_i and the direction of bond ij , and the arrows (\leftrightarrow) and (\updownarrow) in (b) and (c) indicate the elongation direction.

and the corresponding models are also denoted by model 1 and model 2. The difference between models in Eqs. (14), and (15) and Eqs. (2) and (3) comes from the definition of v_{ij} . However, the variables v_{ij} in Eqs. (14) and (15) are identical with v_{ij} in Eqs. (2) and (3) for the nondeformed lattice corresponding to $\xi = 1$ and, therefore, both models in Eqs. (14) and (15) are simple and straightforward extensions of models in Eqs. (2) and (3). From the definitions of v_{ij} in Eqs. (14) and (15), v_{ij} no longer have the meaning of a component of τ_i along or perpendicular to the direction from vertex i to vertex j . It is also possible to start with models 1 and 2 in Eqs. (14) and (15) from the beginning, however, models 1 and 2 in Eqs. (2) and (3) are relatively simple and used to study responses to the external stress \vec{f} in Sec. III A.

Since the definition of v_{ij} in Eqs. (14) and (15) depends on the bond vector \vec{e}'_{ij} , we first show the lattices corresponding to $\xi = 1$, $\xi = 0.9$, and $\xi = 1.1$ in Figs. 14(a)–14(c). Let the bond length or the lattice spacing $a(=|\vec{e}'_{ij}|)$ be $a = 1$ on the regular lattice, then $a(=|\vec{e}'_{ij}|)$ becomes $a > 1$ or $a < 1$ depending on the bond direction on the deformed lattices. For $\xi = 0.9$, all bonds in the horizontal direction, such as bond ij in Fig. 14(b), satisfy $a > 1$, and all other bonds, such as bond ik , satisfy $a < 1$. To the contrary, for $\xi = 1.1$, all bonds in the horizontal direction satisfy $a < 1$ and all other bonds satisfy $a > 1$ as shown in Fig. 14(c).

We should comment on the influences of lattice deformation described in Eqs. (6) on S_{FM} and S_{DM} in models 1 and 2 in detail. First, the definition of S_{DM} initially depends on the lattice shape. Moreover, in S_{DM} of model 2, the influences of lattice deformation come from both \vec{e}'_{ij} and λ_{ij} , which depends on v_{ij} . S_{FM} in model 1 is also dependent on the lattice shape due to this λ_{ij} . In contrast, S_{FM} in model 2 depends only on the connectivity of the lattice and is independent of the lattice shape. To summarize, the lattice deformation by ξ in Eqs. (6) influences both S_{FM} and S_{DM} in model 1, and it influences only S_{DM} in model 2.

Figures 15 and 16 show phase diagrams for the stripe phase in models 1 and 2 under variations of ξ and T . The symbols (Δ), (\circ), and (\square) denote horizontal, isotropic, and vertical alignments of stripe direction. In Fig. 16(g), the alignment direction is not exactly vertical to the horizontal direction, but it is parallel to the triangle's edge directions (see Fig. 1). This deviation in the alignment direction is in contrast to the case

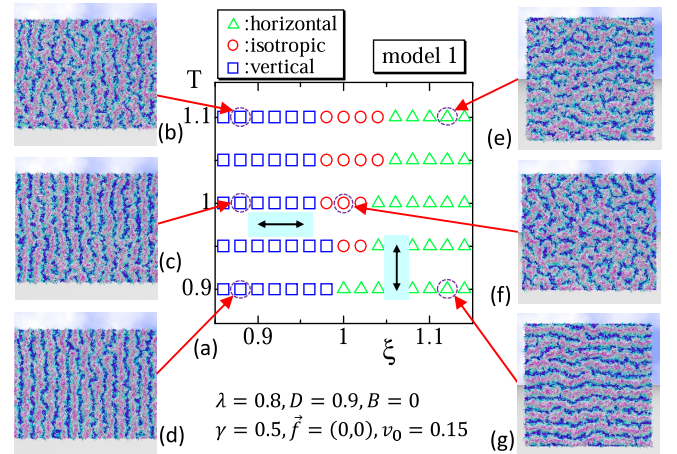


FIG. 15. (a) $T\xi$ diagram in the stripe phase of model 1, where T and ξ are the temperature and deformation parameter in Eqs. (6). The arrows (\leftrightarrow) and (\updownarrow) denote the lattice elongation direction, whereas the symbols (Δ), (\circ), and (\square) denote alignments of the stripe direction. (b)–(d) are snapshots obtained at $\xi = 0.88$ and (e)–(g) are those obtained at $\xi = 1$ and $\xi = 1.12$. The parameters λ and D are the same as those used in Figs. 5 and 11, and (B, γ, f) are fixed to $(B, \gamma, f) = (0, 0.5, 0)$. Fluctuations of spins increase with increasing temperature.

of model 1 in Figs. 15(b)–15(d) and is also in contrast to the case that $\vec{f} = (0, f)$ is applied, where the stripe direction is precisely vertical to the horizontal direction (which is not shown). For $\xi = 1$, the lattice is not deformed, and uniaxial strains, and hence, aligned stripes, are not expected. Indeed, we find from the snapshots in Figs. 15 and 16 that the stripe direction is not always uniformly aligned, except for at relatively low temperatures such as $T = 0.9$. From this, it is reasonable to consider τ to be a strain direction in a

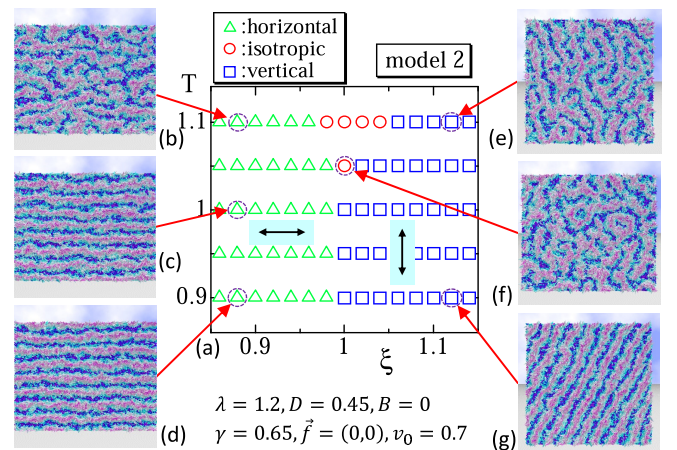


FIG. 16. (a) $T\xi$ diagram in the stripe phase of model 2, where T and ξ are the temperature and deformation parameter in Eqs. (6). The arrows (\leftrightarrow) and (\updownarrow) denote the lattice elongation direction, whereas the symbols (Δ), (\circ), and (\square) denote alignments of the stripe direction. (b)–(d) are snapshots obtained at $\xi = 0.88$, and (e)–(g) are those obtained at $\xi = 1$ and $\xi = 1.12$. The parameters λ and D are the same as those used in Figs. 6 and 12, and (B, γ, f) are fixed to $(B, \gamma, f) = (0, 0.65, 0)$. Fluctuations of spins increase with increasing temperature.

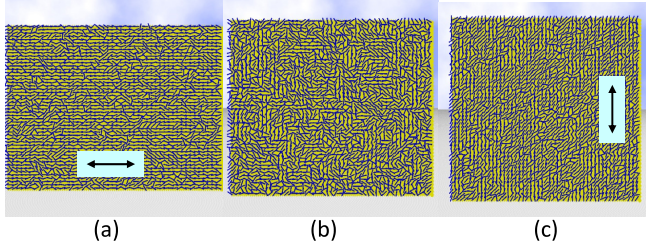


FIG. 17. Snapshots of τ of model 2 obtained at (a) $(T, B) = (0.9, 0.88)$, (b) $(T, B) = (1.05, 1)$, and (c) $(T, B) = (0.9, 1.12)$, which correspond to Figs. 16(d), 16(f), and 16(g), respectively. The small cylinders represent τ . The total number of cylinders is reduced to 2500, which is a quarter of $N (= 10000)$, to clarify the directions. The arrows in (a) (\leftrightarrow) and (c) (\updownarrow) denote the lattice elongation directions.

microscopic sense. If γ is fixed to a larger value, such as $\gamma = 1$ in both models, then the stripe pattern or, equivalently, the direction of τ , becomes anisotropic even at $\xi = 1$ like those in the case of $\xi \neq 1$.

We find that the results of model 2 in Fig. 16 are consistent with the reported experimental data in Ref. [39] (see Fig. 3), implying that τ in model 2 correctly represents the direction of strains expected under the lattice deformations by ξ . On the contrary, the results of model 1 in Fig. 15 are inconsistent with the experimental data. This difference in the stripe direction comes from the fact that the lattice deformation incorrectly influences the alignment of τ or, in other words, τ in model 1 is not considered as the strain direction corresponding to the lattice deformation.

Thus, the strains caused by lattice deformations are consistent (inconsistent) to their stress type, compression, or tension, which determines the direction of stripe pattern in model 2 (model 1) at $T \simeq 1$ and $B = 0$. For the low-temperature region, the responses of lattice deformation in model 2 and model 1 are partly inconsistent with the experimental result in Ref. [39]. To summarize, the numerical results in this paper support that the reason for skyrmion shape deformation, described in Ref. [34], is an anisotropy in the DMI coefficient.

Here we show snapshots of τ in Figs. 17(a)–17(c) corresponding to Figs. 16(d), 16(f), and 16(g), respectively. We find that almost all τ align along the horizontal direction in Fig. 17(a), the direction locally aligns and is globally isotropic in Fig. 17(b), and almost all τ align along the vertical direction or the triangle edge direction in Fig. 17(c). The random state of τ in Fig. 17(b) implies that the direction of the D vector is globally at random and considered to correspond to a noncoplanar distribution of D vectors in the bulk system with inhomogeneous distortion expected from the effective magnetic model [30,31]. Thermal fluctuations in such a random state may grow on larger lattices, and if such an unstable phenomenon is expected, the deformed skyrmion shape changes with increasing lattice size. However, no difference is found in the simulation results on the lattice of size 100×100 and those on the lattices of 200×200 and 400×400 on the dashed lines in Figs. 5 and 6. Due to the competing interactions in our model, the spin configuration is nonuniform with topological textures. However, skyrmion structures cannot be generated by random anisotropies.

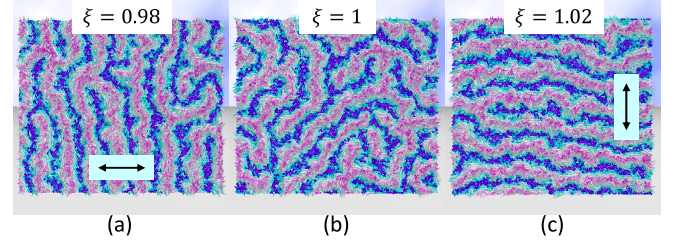


FIG. 18. Responses of the original model, in which the FG prescription is not applied, to the lattice deformations (a) $\xi = 0.98$, (b) $\xi = 1$ and (c) $\xi = 1.02$ in the stripe phase for $(T, \lambda, D, B) = (1, 1.6, 0.9, 0)$. The direction of stripes for $\xi \neq 1$ is inconsistent with the experimental result in Ref. [39]. The arrows inside the snapshots of (a) (\leftrightarrow) and (c) (\updownarrow) denote the lattice elongation direction.

To further check the response of spins to the lattice deformation, we examine the original model defined by [53,54]

$$S = \lambda S_{\text{FM}} + D S_{\text{DM}} - S_B,$$

$$S_{\text{FM}} = \sum_{ij} (1 - \sigma_i \cdot \sigma_j), \quad S_{\text{DM}} = \sum_{ij} \tilde{e}'_{ij} \cdot \sigma_i \times \sigma_j, \quad (16)$$

where both S_{FM} and S_{DM} are not deformed by FG modeling prescription, and S_B is the same as in Eqs. (5). The S_{DM} is defined by using the generalized \tilde{e}'_{ij} in Eq. (13). The parameters are assumed as $(T, \lambda, D, B) = (1, 1.6, 0.9, 0)$. The snapshots are shown in Figs. 18(a)–18(c) for $\xi = 0.98$, $\xi = 1$, and $\xi = 1.02$, respectively. We find that the result is inconsistent with the reported experimental data in Ref. [39]. This inconsistency implies that the effective coupling constants, such as D_x and D_y in Eqs. (4), play a nontrivial role in the skyrmion deformation and the stripe direction. It must also be emphasized that the stress effect implemented in model 2 via the alignment of τ correctly influences helical spin configurations of the skyrmion shape deformation and the stripe direction.

For smaller (larger) ξ , such as $\xi = 0.94$ ($\xi = 1.06$), the vertical (horizontal) direction of stripes becomes more apparent in Fig. 18. Interestingly, the vertical direction of stripes is parallel to the y direction and not parallel to the triangle edge directions. This result indicates that the vertical direction shown in Fig. 16(g) comes from nontrivial effects of λ_{ij} of S_{FM} and S_{DM} in Eqs. (14) and (15). We note that the parameters are not always limited to those used in Fig. 18. It is possible to use a wide range of (T, λ, D) where isotropic stripe configurations like in Fig. 18(b) are expected for $\xi = 1$. In Fig. 19(a), the Finsler length v_{ij} defined by Eqs. (14) for $\xi = 0.9$ are plotted, where the horizontal axis θ is the angle between τ_i and \tilde{e}'_{ij} [see Fig. 14(a)]. For $\xi = 1$, v_{ij} (dashed line) is identical with the original v_{ij} in Eqs. (2), which is also plotted (solid line) and is found to be shifted from $[0, 1]$ to $[v_0, 1 + v_0]$ by a constant $v_0 (= 0.15)$ in Figs. 19(a) and 19(b) and $v_0 (= 0.7)$ in Figs. 19(c) and 19(d). We find that v_{ij} (dashed line) deviates from v_{ij} (solid line) only slightly at the region $\theta \rightarrow 0$ or, equivalently, $\theta \rightarrow \pi$, while at $\theta \rightarrow \pi/2$, v_{ij} (dashed line) is identified with v_{ij} (solid line) for any ξ . On the lattice of $\xi = 1.1$ in Fig. 19(b), the behavior of v_{ij} (dashed line) is almost comparable to the case of $\xi = 0.9$ in Fig. 19(a). In addition, the curve of v_{ij} (dashed line) of model 2 on the long bond $a > 1$ also includes a constant part ($= v_0$) at $\theta \rightarrow 0$ like in the

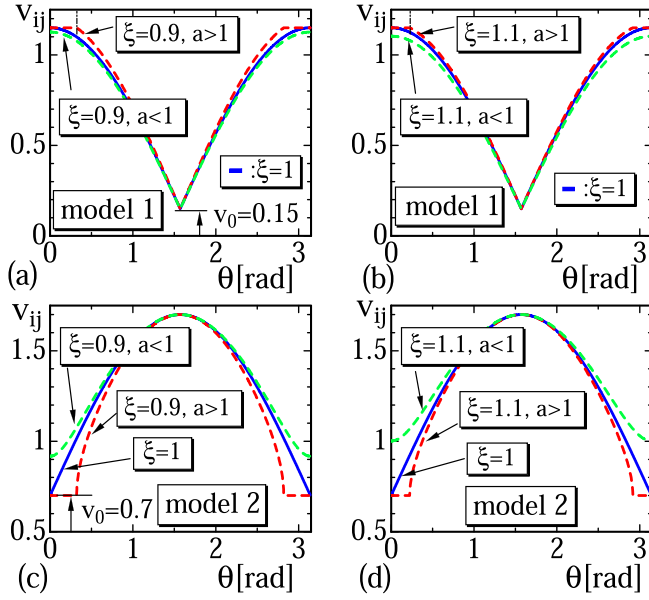


FIG. 19. The variation of v_{ij} versus θ of model 1 for (a) $\xi=0.9$ and (b) $\xi=1.1$, and v_{ij} versus θ of model 2 for (c) $\xi=0.9$ and (d) $\xi=1.1$, where θ is the angle between τ_i and \vec{e}'_{ij} [see Fig. 14(a)]. All the curves of v_{ij} (dashed lines) continuously reduce to the curve of v_{ij} (solid line) in the limit of $\xi \rightarrow 1$.

case of model 1. This constant part disappears in the limit of $\xi \rightarrow 1$, and hence, model 2 in Eqs. (15) as well as model 1 in Eqs. (14) is understood to be an extension of those in Eqs. (2) and (3) as mentioned above. Now we discuss why the results of model 2 are considered to be more realistic. We show the variation of effective coupling constants λ_μ and D_μ ($\mu=x, y$), defined by Eqs. (4), with respect to ξ [Figs. 20(a) and 20(b)], where the anisotropies η_λ and η_D , defined by Eqs. (12), are also plotted. We find that in the region $\xi > 1$, both η_λ and η_D are decreasing and smaller than those in $\xi < 1$ in Figs. 20(a) and 20(b). Remarkably, the variations of D_x , D_y , and η_D versus ξ in model 2 almost discontinuously change at $\xi = 1$ and are in sharp contrast to those of model 1. In model 2, if η_D is positive (negative), which implies $D_x < D_y$ ($D_x > D_y$),

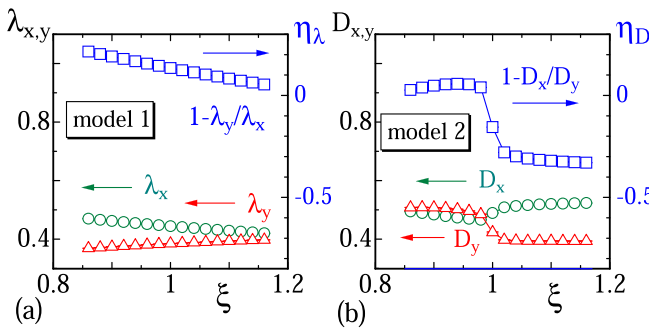


FIG. 20. (a) The effective coupling constants λ_x , λ_y and the anisotropy η_λ versus ξ of model 1, and (b) D_x , D_y and η_D of model 2. The behaviors of λ_μ and η_λ of model 1 are almost identical to those of model 2 except the jumps at $\xi = 1$ in model 2. These data of model 1 (model 2) are obtained from the simulations in Fig. 15 (Fig. 16) at $T = 1$.

then the stripe direction is horizontal (vertical). Thus, we find that model 2 on the deformed lattices for $\xi < 1$ [Fig. 14(b)] shares the same property as that on the nondeformed lattice with a tensile stress $\vec{f} = (f, 0)$. Indeed, the stripe direction of model 2 is horizontal [Fig. 6(f)] and η_D is positive [Fig. 9(d)] under the tensile stress of the horizontal direction $\vec{f} = (f, 0)$. In other words, the response of model 2 on the nondeformed lattice with uniaxial stress $\vec{f} = (f, 0)$ is the same as that on the deformed lattice in Fig. 14(b) corresponding to $\xi < 1$. This is considered to be the reason why model 2 provides the consistent result of stripe direction with experimental data.

From these observations, we find that the small value region of v_{ij} plays an important role in the model's response. The small value region in model 1 is $\theta \simeq \pi/2$ [Figs. 19(a) and 19(b)], where τ_i is almost vertical to \vec{e}'_{ij} , and v_{ij} for $\xi \neq 1$ is almost the same as v_{ij} for $\xi = 1$ and, therefore, no new result is expected in model 1. In contrast, the small value region in model 2 is $\theta \simeq 0$ [Figs. 19(c) and 19(d)], where τ_i is almost parallel to \vec{e}'_{ij} , and even a small deviation of v_{ij} (dashed line) from v_{ij} (solid line) is relevant. Such a nontrivial behavior of model 2 emerging from the small v_{ij} region is understood from the fact that the effective coupling constant λ_{ij} is given by a rational function of v_{ij} .

We should emphasize that the result, supporting that model 2 is consistent with both skyrmion deformation and stripe direction, is obtained by comparing models 1 and 2, and that the result of model 2 is consistent with that in Ref. [33], where an additional energy term for MEC is included in a Landau-Ginzburg free energy. In this additional interaction term, strains and magnetization are directly coupled. In our models, the strain field τ is introduced in S_f , and τ represents strain direction, though S_f includes no direct interaction of τ and magnetization or spin variable σ . Thus, we consider that model 2 supports the model in Ref. [34], where an anisotropy in the DMI coefficient is explicitly assumed, implying that uniaxial stress deforms DMI anisotropic.

Another choice is that both FMI and DMI are modified by FG modeling prescription. This model is certainly expected to reproduce the experimentally observed shape deformation of skyrmions. However, this choice is not suitable for reproducing the stripe direction alignment by lattice deformation because model 1 is contradictory for this purpose, as demonstrated above. Therefore, we eliminate this choice from suitable models and find the conclusion stated above.

IV. SUMMARY AND CONCLUSION

Using a FG model on a 2D triangular lattice with periodic boundary conditions, we numerically study skyrmion deformation under uniaxial stress and the lattice deformation. Two different models, models 1 and 2, are examined: the ferromagnetic energy S_{FM} and Dzyaloshinskii-Moriya energy S_{DM} are deformed by FG modeling prescription in models 1 and 2, respectively. In these FG models, the coupling constants λ and D of S_{FM} and S_{DM} are dynamically deformed to be direction dependent such that $\lambda_x \neq \lambda_y$ and $D_x \neq D_y$. In both models, the ratio λ/D is dynamically distorted to be direction dependent with an internal degree of freedom τ for strains and a mechanical force or stress \vec{f} .

We find that the results of both models for skyrmion deformation under uniaxial stress are consistent with the reported experimental data. For the direction of stripes as a response to the stresses, the numerical data of both models are also consistent with the reported experimental result observed at room temperature with zero magnetic field. However, we show that the responses of the two models to lattice deformations are different from each other in the stripe phase. In this case, only the data obtained by model 2 are shown to be consistent with the experimental result. We conclude that in real systems only lattice deformations due to the DMI are relevant. Note that the original model, in which both FMI and DMI energies are not deformed by FG modeling prescription, is also examined under the lattice deformations and the produced stripe directions are found to be different from those of the experimental data. This shows that the lattice deformations naturally introduced into the system by the FG modeling are necessary to explain the experimental results.

Combining the obtained results for responses to both uniaxial stresses and lattice deformations, we conclude that the anisotropy of the DMI coefficient is considered to be the origin of the experimentally observed and reported skyrmion deformations by uniaxial mechanical stresses. Thus, the FG modeling can provide a successful model to describe modulated chiral magnetic excitations on thin films caused by the anisotropy in the ratios λ/D .

ACKNOWLEDGMENTS

This study was initiated during a two-month stay of S.E.H. at Ibaraki KOSEN in 2017, and this stay was financially supported in part by Techno AP Co. Ltd., Genesis Co. Ltd., Kadowaki Sangyo Co. Ltd, and also by JSPS KAKENHI Grant No. JP17K05149. H.K. acknowledges V. Egorov for simulation tasks in the early stage of this work during a four-month stay from 2019 to 2020 at Sendai KOSEN. The simulations and data analyses were performed with S. Tamano, S. Sakurai, and Y. Tanaka's assistance. This work is supported in part by JSPS Grant-in-Aid for Scientific Research on Innovative Areas Discrete Geometric Analysis for Materials Design, Grant No. 20H04647.

APPENDIX A: FINSLER GEOMETRY MODELING OF FERROMAGNETIC AND DZYALOSHINSKII-MORIYA INTERACTIONS

In this Appendix A, we show detailed information on how the discrete forms of S_{FM} and S_{DM} in Eqs. (2) and (3) are obtained. To simplify descriptions, we focus on the models on nondeformed lattices in Eqs. (2) and (3). Note that descriptions of models on deformed lattices in Eqs. (14) and (15) remain unchanged except the definition of v_{ij} . Let us start with the continuous form of S_{FM} . Since the variable σ ($\in S^2$: unit sphere) is defined on a two-dimensional surface, the continuous S_{FM} and S_{DM} are given by

$$\begin{aligned} S_{\text{FM}} &= \frac{1}{2} \int \sqrt{g} d^2x g^{ab} \frac{\partial \sigma}{\partial x^a} \cdot \frac{\partial \sigma}{\partial x^b}, \\ S_{\text{DM}} &= \int \sqrt{g} d^2x g^{ab} \frac{\partial \vec{r}}{\partial x^a} \cdot \sigma \times \frac{\partial \sigma}{\partial x^b}, \end{aligned} \quad (\text{A1})$$

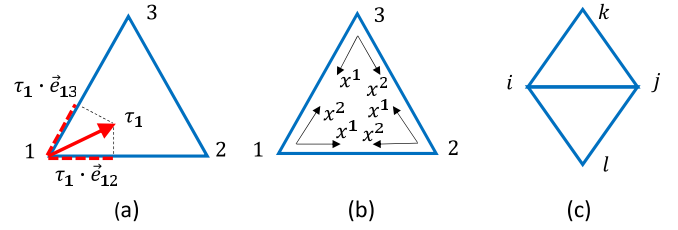


FIG. 21. (a) A triangle of vertices 123 and a strain field τ_1 at vertex 1, and its tangential components $\tau_1 \cdot \vec{e}_{12}$ and $\tau_1 \cdot \vec{e}_{13}$ along the directions \vec{e}_{12} and \vec{e}_{13} , which are the unit tangential vectors from vertices 1 to 2 and 1 to 3. (b) Three possible local coordinates on the triangle 123, (c) two neighboring triangles ijk and jil .

where g^{ab} is the inverse of the metric g_{ab} , and g is its determinant (see also Ref. [54]). Note that the unit tangential vector \vec{e}_a can be used for $\partial \vec{r} / \partial x^a$, which is not always a unit vector. Indeed, the difference between \vec{e}_a and $\partial \vec{r} / \partial x^a$ is a constant multiplicative factor on the regular triangular lattice, and therefore, we use \vec{e}_a for $\partial \vec{r} / \partial x^a$ for simplicity. For simulations on deformed lattices, this unit vector \vec{e}_a is replaced by a more general one \vec{e}'_a in Eq. (13).

Here we assume that g_{ab} is not always limited to the induced metric $(\partial \vec{r} / \partial x^i) \cdot (\partial \vec{r} / \partial x^j)$ but is assumed to be of the form

$$g_{ab} = \begin{pmatrix} v_{12}^{-2} & 0 \\ 0 & v_{13}^{-2} \end{pmatrix} \quad (\text{A2})$$

on the triangle of vertices 123 [see Fig. 21(a)], where v_{ij} is defined by using the strain field τ_i ($\in S^1$: unit circle) such that

$$\begin{aligned} v_{ij} &= |\tau_i \cdot \vec{e}_{ij}| + v_0, \quad (\text{for } S_{\text{FM}}; \text{ model 1}), \\ v_{ij} &= \sqrt{1 - (\tau_i \cdot \vec{e}_{ij})^2} + v_0, \quad (\text{for } S_{\text{DM}}; \text{ model 2}). \end{aligned} \quad (\text{A3})$$

Note that the definition of v_{ij} in S_{FM} in model 1 is different from that in S_{DM} in model 2.

We should comment that the usage of FG in this paper for chiral magnetism is not the standard one of non-Euclidean geometry such as in Ref. [55]. In the case of Ref. [55], a nonflat geometry is assumed to describe real curved thin films in \mathbf{R}^3 and to extract curvature effect on a magnetic system. In contrast, the film in this paper is flat and follows Euclidean geometry; however, an additional distance called Finsler length is introduced to describe Hamiltonian S_{FM} or S_{DM} . Even when the surface is curved, in which the surface geometry follows the induced metric or Euclidean geometry in \mathbf{R}^3 as in Ref. [55], a Finsler length can also be introduced in addition to the surface geometry. Such a non-Euclidean length scale can constantly be introduced to the tangential space, where the length of the vector or the distance of two different points is defined by the newly introduced metric tensor such as g_{ab} in Eq. (A2). Therefore, in the FG modeling prescription, we have two different length scales; one is the Euclidean length for thin films in \mathbf{R}^3 and the other is dynamically changeable Finsler length for Hamiltonian.

The Finsler length scale is used to effectively deform the coefficient λ_{ij} in Eqs. (2) and (3), which will be described below in detail. This λ_{ij} varies depending on the internal strain variable τ , which is integrated out in the partition function

and, therefore, all physical quantities are effectively integrated over different length scales characterized by the ratio λ/D of interaction coefficients for FMI and DMI. Here, this ratio is fluctuating and its mean value can be observed and expressed by using the effective coupling constant in Eqs. (4). Thus, dynamically deformed D means that all-important length scales are effectively integrated out with the Boltzmann weight to calculate observable quantities. Note that this is possible if g_{ab} is treated to be dynamically changeable. For this reason, this FG modeling is effective, especially for anisotropic phenomena, because we can start with isotropic models such as the isotropic FMI and DMI. Therefore, the FG model is in sharp contrast to those models with explicit anisotropic interaction terms such as Landau-type theory for MEC. This FG modeling is a coarse-grained one like the linear chain model, of which the connection to monomers is mathematically confirmed [56]. In such a coarse-grained modeling, the detailed information on electrons and atoms is lost from the beginning, like in the case of FMI. In other words, no specific information at the scale of atomic level is necessary to calculate physical quantities even in such complex anisotropic phenomena.

To obtain the discrete expressions of S_{FM} , we replace $\int \sqrt{g} d^2x \rightarrow \sum_{\Delta} (1/v_{12}v_{13})$ and $g^{11} \partial \sigma / \partial x^1 \cdot \partial \sigma / \partial x^1 \rightarrow v_{12}^2 (\sigma_2 - \sigma_1)^2$, $g^{22} \partial \sigma / \partial x^2 \cdot \sigma / \partial x^2 \rightarrow v_{13}^2 (\sigma_3 - \sigma_1)^2$ on the triangle of vertices 123 [Fig. 21(a)], where the local coordinate origin is at vertex 1, and \sum_{Δ} denotes the sum over triangles. The discrete form of S_{DM} is also obtained by the replacements $g^{11} \partial \vec{r} / \partial x^1 \cdot (\sigma \times \partial \sigma / \partial x^1) \rightarrow v_{12}^2 \mathbf{e}_{12} \cdot (\sigma_1 \times \sigma_2)$, $g^{22} \partial \vec{r} / \partial x^2 \cdot (\sigma \times \partial \sigma / \partial x^2) \rightarrow v_{13}^2 \mathbf{e}_{13} \cdot (\sigma_1 \times \sigma_3)$. Then, we have

$$S_{\text{FM}} = \frac{1}{2} \int \sqrt{g} d^2x \left(g^{11} \frac{\partial \sigma}{\partial x^1} \cdot \frac{\partial \sigma}{\partial x^1} + g^{22} \frac{\partial \sigma}{\partial x^2} \cdot \frac{\partial \sigma}{\partial x^2} \right) \rightarrow \sum_{\Delta} \left[\frac{v_{12}}{v_{13}} (1 - \sigma_1 \cdot \sigma_2) + \frac{v_{13}}{v_{12}} (1 - \sigma_1 \cdot \sigma_3) \right] \quad (\text{A4})$$

and

$$S_{\text{DM}} = \int \sqrt{g} d^2x \left(g^{11} \frac{\partial \vec{r}}{\partial x^1} \cdot \sigma \times \frac{\partial \sigma}{\partial x^1} + g^{22} \frac{\partial \vec{r}}{\partial x^2} \cdot \sigma \times \frac{\partial \sigma}{\partial x^2} \right) \rightarrow \sum_{\Delta} \left[\frac{v_{12}}{v_{13}} (\vec{e}_{12} \cdot \sigma_1 \times \sigma_2) + \frac{v_{13}}{v_{12}} (\vec{e}_{13} \cdot \sigma_1 \times \sigma_3) \right]. \quad (\text{A5})$$

The local coordinate origin can also be assumed at vertices 2 and 3 on the triangle 123 (Fig. 21(b)). Therefore, summing over the discrete expressions of S_{FM} and S_{DM} for the three possible local coordinates, which are obtained by replacing the indexes $1 \rightarrow 2, 2 \rightarrow 3, \dots$ with the factor $1/3$, we have

$$S_{\text{FM}} = \frac{1}{3} \sum_{\Delta} \left[\left(\frac{v_{12}}{v_{13}} + \frac{v_{21}}{v_{23}} \right) (1 - \sigma_1 \cdot \sigma_2) + \left(\frac{v_{23}}{v_{21}} + \frac{v_{32}}{v_{31}} \right) (1 - \sigma_2 \cdot \sigma_3) + \left(\frac{v_{13}}{v_{12}} + \frac{v_{31}}{v_{32}} \right) (1 - \sigma_3 \cdot \sigma_1) \right] \quad (\text{A6})$$

and

$$S_{\text{DM}} = \frac{1}{3} \sum_{\Delta} \left[\left(\frac{v_{12}}{v_{13}} + \frac{v_{21}}{v_{23}} \right) (\vec{e}_{12} \cdot \sigma_1 \times \sigma_2) \right]$$

$$+ \left(\frac{v_{23}}{v_{21}} + \frac{v_{32}}{v_{31}} \right) (\vec{e}_{23} \cdot \sigma_2 \times \sigma_3) + \left(\frac{v_{13}}{v_{12}} + \frac{v_{31}}{v_{32}} \right) (\vec{e}_{31} \cdot \sigma_3 \times \sigma_1) \Big]. \quad (\text{A7})$$

Replacing the vertices 1,2,3 with i, j, k , we have the following expressions for S_{FM} and S_{DM} such that:

$$S_{\text{FM}} = \sum_{\Delta} [\lambda_{ij}(1 - \sigma_i \cdot \sigma_j) + \lambda_{jk}(1 - \sigma_j \cdot \sigma_k) + \lambda_{ki}(1 - \sigma_k \cdot \sigma_i)],$$

$$S_{\text{DM}} = \sum_{\Delta} [\lambda_{ij}(\vec{e}_{ij} \cdot \sigma_i \times \sigma_j) + \lambda_{jk}(\vec{e}_{jk} \cdot \sigma_j \times \sigma_k) + \lambda_{ki}(\vec{e}_{ki} \cdot \sigma_k \times \sigma_i)],$$

$$\lambda_{ij} = \frac{1}{3} \left(\frac{v_{ij}}{v_{ik}} + \frac{v_{ji}}{v_{jk}} \right), \quad (\text{A8})$$

where k in λ_{ij} is the third vertex number other than i and j . Note that $\lambda_{ij} = \lambda_{ji}$ is satisfied.

The sum over triangles \sum_{Δ} in these expressions can also be replaced by the sum over bonds \sum_{ij} , and we also have

$$S_{\text{FM}} = \sum_{ij} \bar{\lambda}_{ij} (1 - \sigma_i \cdot \sigma_j), \quad S_{\text{DM}} = \sum_{ij} \bar{\lambda}_{ij} (\mathbf{e}_{ij} \cdot \sigma_i \times \sigma_j), \quad (\text{A9})$$

where the coefficients $\bar{\lambda}_{ij}$ on the triangles are given by

$$\bar{\lambda}_{ij} = \frac{1}{3} \left(\frac{v_{ij}}{v_{ik}} + \frac{v_{ji}}{v_{jk}} + \frac{v_{il}}{v_{il}} + \frac{v_{jl}}{v_{jl}} \right). \quad (\text{A10})$$

In this expression, the vertices k and l are those connected with i and j [see Fig. 21(c)]. The coefficient $\bar{\lambda}_{ij}$ is also symmetric; $\bar{\lambda}_{ij} = \bar{\lambda}_{ji}$, where k and l should also be replaced by each other if i is replaced by j . For numerical implementation, the expressions in the sum of triangles are easier than the sum over bonds, and we use the sum over triangles in the simulations in this paper.

Now, the origin of the form of g_{ab} in Eq. (A2) is briefly explained [57–60]. Let $L(x(t), y(t))$ be a Finsler function on a two-dimensional surface defined by

$$L(x(t), y(t)) = \sqrt{(y^1)^2 + (y^2)^2} / |\vec{v}| = \sqrt{\left(\frac{dx^1}{dt} \right)^2 + \left(\frac{dx^2}{dt} \right)^2} / |\vec{v}|, |\vec{v}| = \sqrt{\left(\frac{dx^1}{ds} \right)^2 + \left(\frac{dx^2}{ds} \right)^2}, \quad \vec{v} = \left(\frac{dx^1}{ds}, \frac{dx^2}{ds} \right), \quad (\text{A11})$$

where \vec{v} is a velocity along C other than $y(t) = (dx^1/dt, dx^2/dt)$, and \vec{v} is assumed to be identical to the derivative of (x^1, x^2) with respect to the parameter s [Fig. 22(a)]. It is easy to check that

$$s = \int_{t_0}^t L(x(t), y(t)) dt \quad \left(\Leftrightarrow \frac{ds}{dt} = L(x(t), y(t)) \right), \quad (\text{A12})$$

and this s is called *Finsler length* along the positive direction of C . The Finsler metric g_{ab} , ($a, b = 1, 2$), which is a 2×2

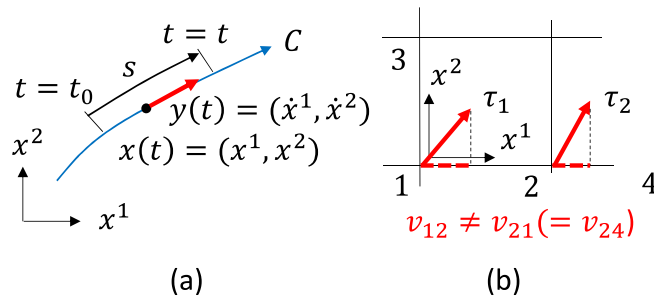


FIG. 22. (a) A curve C parameterized by t on a two-dimensional continuous surface, where a point $x(t) = (x^1, x^2)$ on C and its derivative $y(t) = (\dot{x}^1, \dot{x}^2)$ are represented by a local coordinate. (b) A regular square lattice with a local coordinate axes x^1 and x^2 at vertex 1 and strain fields $\tau_i (i=1, 2)$ at vertices 1 and 2. Note that $v_{12} \neq v_{21} (= v_{24})$, implying that the velocity from 1 to 2 is different from the velocity from 2 to 1, while $v_{21} = v_{24}$.

matrix, is given by using the Finsler function such that

$$g_{ab} = \frac{1}{2} \frac{\partial^2 L}{\partial y^a \partial y^b}. \quad (\text{A13})$$

Now, let us consider the Finsler function $L(x, y)$ on the square lattice (for simplicity). Note that L is defined only on the local coordinate axes on the lattice, and therefore we have

$$L(x(t), y(t)) = y^1 / v_{12} \quad (\text{A14})$$

on x^1 axis from vertices 1 to 2 [Fig. 22(b)], where v_{12} is the velocity from vertex 1 to vertex 2 defined in Eqs. (A3). From this expression and Eq. (A13), we have $g_{11} = v_{12}^{-2}$. We also have $g_{22} = v_{13}^{-2}$ from the Finsler function $L = y^2 / v_{13}$ defined on x^2 axis from vertex 1 to vertex 3. Thus, we have the discrete and local coordinate expression of Finsler metric in Eq. (A2) on square lattices shown in Fig. 22(b), though the expression of g_{ab} in Eq. (A2) for triangular lattices. Indeed, on triangular lattices, the expression of g_{ab} is the same as that on square lattices, and the only difference is that there are three possible local coordinates on triangles, while there are four possible local coordinates on squares. Due to this difference,

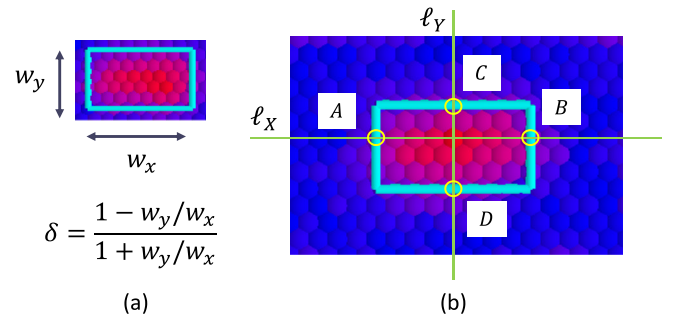


FIG. 23. (a) The definition of shape anisotropy δ with a snapshot of skyrmion enclosed by a rectangle for the graphical measurement of w_x and w_y , and (b) two lines ℓ_x and ℓ_y , passing through the local minimum of σ_z , are used to find the four points A, B, C , and D for the rectangle.

the coefficient λ_{ij} in Eqs. (A8) becomes slightly different from that on square lattices; however, we have no difference in the expression of g_{ab} for the dependence on the lattice structure.

APPENDIX B: GRAPHICAL MEASUREMENT OF SKYRMION SHAPE ANISOTROPY

Here we describe how to measure the side lengths w_x and w_y of a skyrmion for the shape anisotropy δ [Fig. 23(a)], where a snapshot of the skyrmion is shown simply by two-color gradation in blue and red using $\sigma_z \in [-1, 1]$. Two lines ℓ_x and ℓ_y in Fig. 23(b) are drawn parallel to the x and y directions, and the point where two lines cross is a vertex where σ_z is the local minimum (or maximum depending on the direction of \vec{B}). This local minimum σ_z is numerically determined to be smaller than those of the four nearest-neighbor vertices in all directions. The point A is the first vertex, where the sign of σ_z changes from minus to plus, encountered moving along ℓ_x from the crossing point. The other vertex B is also uniquely determined in the same way. Note that the crossing point is not always located at the center of A and B on ℓ_x . The vertices C and D on ℓ_y are also uniquely determined. The values of σ_z at these four points A, B, C , and D are not always exactly identical to $\sigma_z = 0$ but are small positive close to $\sigma_z = 0$.

[1] T. H. R. Skyrme, *Proc. Royal Soc. London, Ser. A* **260**, 127 (1961).
[2] T. Moriya, *Phys. Rev.* **120**, 91 (1960).
[3] I. E. Dzyaloshinskii, *J. Exptl. Theoret. Phys. (U.S.S.R.)* **46**, 1420 (1964) [*Sov. Phys. JETP* **19**, 960 (1964)].
[4] U. K. Rössler, A. N. Bogdanov, and C. Pfleiderer, *Nature (London)* **442**, 797 (2006).
[5] A. N. Bogdanov, U. K. Rössler, and C. Pfleiderer, *Phys. B* **359**, 1162 (2005).
[6] A. N. Bogdanov and D. A. Yablonskii, *Zh. Eksp. Teor. Fiz.* **95**, 178 (1989) [*Sov. Phys. JETP* **68**, 101 (1989)].
[7] M. Uchida, Y. Onose, Y. Matsui, and Y. Tokura, *Science* **311**, 359 (2006).
[8] X. Yu, Y. Onose, N. Kanazawa, J. H. Park, J. H. Han, Y. Matsui, N. Nagaosa, and Y. Tokura, *Nature (London)* **465**, 901 (2010).

[9] S. Mühlbauer, B. Binz, F. Jonietz, C. Pfleiderer, A. Rosch, A. Neubauer, R. Georgii 1, and P. Böni, *Science* **323**, 915 (2009).
[10] W. Munzer, A. Neubauer, T. Adams, S. Mühlbauer, C. Franz, F. Jonietz, R. Georgii, P. Boni, B. Pedersen, M. Schmidt, A. Rosch, and C. Pfleiderer, *Phys. Rev. B* **81**, 041203(R) (2010).
[11] X. Yu, M. Mostovoy, Y. Tokunaga, W. Zhang, K. Kimoto, Y. Matsui, Y. Kaneko, N. Nagaosa, and Y. Tokura, *Proc. Natl. Acad. Sci. USA* **109**, 8856 (2012).
[12] A. Fert, N. Reyren, and V. Cros, *Nat. Rev.* **2**, 17031 (2017).
[13] N. Romming, C. Hanneken, M. Menzel, J. A. E. Bickel, B. Wolter, K. von Bergmann, A. Kubetzka, and R. Wiesendanger, *Science* **341**, 636 (2013).
[14] S. Buhrandt and L. Fritz, *Phys. Rev. B* **88**, 195137 (2013).
[15] Y. Zhou and M. Ezawa, *Nat. Comm.* **5**, 4652 (2014).

- [16] J. Iwasaki, M. Mochizuki, and N. Nagaosa, *Nat. Comm.* **4**, 1463 (2013).
- [17] S. Banerjee, J. Rowland, O. Erten, and M. Randeria, *Phys. Rev. X* **4**, 031045 (2014).
- [18] U. Güngördü, R. Nepal, O. A. Tretiakov, K. Belashchenko, and A. A. Kovalev, *Phys. Rev. B* **93**, 064428 (2016).
- [19] A. Chacon, A. Bauer, T. Adams, F. Rucker, G. Brandl, R. Georgii, M. Garst, and C. Pfleiderer, *Phys. Rev. Lett.* **115**, 267202 (2015).
- [20] A. I. Levatić, P. Popčević, V. Šurija, A. Kruchkov, H. Berger, A. Magrez, J. S. White, H. M. Ronnow, and I. Živković, *Sci. Rep.* **6**, 21347 (2016).
- [21] A. N. Bogdanov and U. K. Röβler, *Phys. Rev. Lett.* **87**, 037203 (2001).
- [22] A. B. Butenko, A. A. Leonov, U. K. Rossler, and A. N. Bogdanov, *Phys. Rev. B* **82**, 052403 (2010).
- [23] S. Seki, Y. Okamura, K. Shibata, R. Takagi, N. D. Khanh, F. Kagawa, T. Arima, and Y. Tokura, *Phys. Rev. B* **96**, 220404(R) (2017).
- [24] X. Yu, A. Kikkawa, D. Morikawa, K. Shibata, Y. Tokunaga, Y. Taguchi, and Y. Tokura, *Phys. Rev. B* **91**, 054411 (2015).
- [25] R. Ritz, M. Halder, C. Franz, A. Bauer, M. Wagner, R. Bamler, A. Rosch, and C. Pfleiderer, *Phys. Rev. B* **87**, 134424 (2013).
- [26] Y. Shi and J. Wang, *Phys. Rev. B* **97**, 224428 (2018).
- [27] Y. Nii, A. Kikkawa, Y. Taguchi, Y. Tokura, and Y. Iwasa, *Phys. Rev. Lett.* **113**, 267203 (2014).
- [28] Y. Nii, T. Nakajima, A. Kikkawa, Y. Yamasaki, K. Ohishi, J. Suzuki, Y. Taguchi, T. Arima, Y. Tokura, and Y. Iwasa, *Nat. Comm.* **6**, 8539 (2015).
- [29] J. Chen, W. P. Cai, M. H. Qin, S. Dong, X. B. Lu, X. S. Gao, and J.-M. Liu, *Sci. Rep.* **7**, 7392 (2017).
- [30] M. L. Plumer and M. B. Walker, *J. Phys. C: Solid State Phys.* **15**, 7181 (1982).
- [31] E. Franus-Muir, M. L. Plumer, and E. Fawcett, *J. Phys. C: Solid State Phys.* **17**, 1107 (1984).
- [32] M. Kataoka, *J. Phys. Soc. Jpn.* **56**, 3635 (1987).
- [33] J. Wang, Y. Shi, and M. Kamlah, *Phys. Rev. B* **97**, 024429 (2018).
- [34] K. Shibata, J. Iwasaki, N. Kanazawa, S. Aizawa, T. Tanigaki, M. Shirai, T. Nakajima, M. Kubota, M. Kawasaki, H. S. Park, D. Shindo, N. Nagaosa, and Y. Tokura, *Nat. Nanotech.* **10**, 589 (2015).
- [35] T. Koretsune, N. Nagaosa, and R. Arita, *Sci. Rep.* **75**, 13302 (2015).
- [36] S. A. Osorio, M. B. Sturla, H. D. Rosales, and D. C. Cabra, *Phys. Rev. B* **100**, 220404(R) (2019).
- [37] S. Gao, H. D. Rosales, F. A. G. Albarracín, V. Tsurkan, G. Kaur, T. Fennell, P. Steffens, M. Boehm, P. Čermák, A. Schneidewind, E. Ressouche, D. C. Cabra, C. Rüegg, and O. Zaharko, *Nature* **586**, 37 (2020).
- [38] E. Y. Vedmedenko, A. Kubetzka, K. von Bergmann, O. Pietzsch, M. Bode, J. Kirschner, H. P. Oepen, and R. Wiesendanger, *Phys. Rev. Lett.* **92**, 077207 (2004).
- [39] J. Dho, Y. N. Kim, Y. S. Hwang, J. C. Kim, and N. H. Hur, *Appl. Phys. Lett.* **82**, 1434 (2003).
- [40] Y. Takano and H. Koibuchi, *Phys. Rev. E* **95**, 042411 (2017).
- [41] E. Proutorov, N. Matsuyama, and H. Koibuchi, *J. Phys. C* **30**, 405101 (2018).
- [42] V. Egorov, O. Maksimova, H. Koibuchi, C. Bernard, J.-M. Chenal, O. Lame, G. Diguët, G. Sebald, J.-Y. Cavaille, and T. Takagi, *Phys. Lett. A* **396**, 127230 (2021).
- [43] H. Koibuchi, S. El Hog, V. Egorov, F. Kato, and H. T. Diep, *J. Phys. Conf. Ser.* **1391**, 012013 (2019).
- [44] M. Creutz, *Quarks, Gluons and Lattices* (Cambridge University Press, Cambridge, 1983).
- [45] T. Okubo, S. Chung, and H. Kawamura, *Phys. Rev. Lett.* **108**, 017206 (2012).
- [46] H. D. Rosales, D. C. Cabra, and P. Pujol, *Phys. Rev. B* **92**, 214439 (2015).
- [47] P. A. Lebowhl and G. Lasher, *Phys. Rev. A* **6**, 426 (1972).
- [48] N. Metropolis, A. W. Rosenbluth, M. N. Rosenbluth, and A. H. Teller, *J. Chem. Phys.* **21**, 1087 (1953).
- [49] D. P. Landau, *Phys. Rev. B* **13**, 2997 (1976).
- [50] S. El Hog, A. Bailly-Reyre, and H. T. Diep, *J. Mag. Mat.* **455**, 32 (2018).
- [51] A. O. Leonov, T. L. Monchesky, N. Romming, A. Kubetzka, A. N. Bogdanov, and R. Wiesendanger, *New J. Phys.* **18**, 065003 (2016).
- [52] M. Janoschek, M. Garst, A. Bauer, P. Krautscheid, R. Georgii, P. Böoni, and C. Pfleiderer, *Phys. Rev. B* **87**, 134407 (2013).
- [53] S. El Hog, F. Kato, H. Koibuchi, and H. T. Diep, *J. Mag. Mag. Mat.* **498**, 166095 (2020).
- [54] H. T. Diep and H. Koibuchi, Frustrated magnetic thin films: Spin waves and skyrmions in *Frustrated Spin Systems*, 3rd ed., edited by H. T. Diep (World Scientific, Singapore, 2020).
- [55] Y. Gaididei, V. P. Kravchuk, and D. D. Sheka, *Phys. Rev. Lett.* **112**, 257203 (2014).
- [56] M. Doi and S. F. Edwards, *The Theory of Polymer Dynamics* (Oxford University Press, Oxford, United Kingdom, 1986).
- [57] S.-S. Chern, Finsler geometry is just riemannian geometry without the quadratic restriction, in *Notices of the AMS* (American Mathematical Society, Providence, 1996), pp. 959-963.
- [58] M. Matsumoto, *Keiryō Bibun Kikagaku (in Japanese)* (Shokabo, Tokyo 1975).
- [59] D. Bao, S.-S. Chern, Z. Shen, *An Introduction to Riemann-Finsler Geometry*, Graduate Texts in Mathematics Vol. 200 (Springer, New York, 2000).
- [60] H. Koibuchi and H. Sekino, *Physica A* **393**, 37 (2014).